ROYAL SOCIETY OF CHEMISTRY

PAPER

Check for updates

Theoretical modeling of contact-separation mode triboelectric nanogenerators from initial charge distribution†

Hongfa Zhao,‡[a] Hao Wang,‡[b] Hongyong Yu,[b] Qinghao Xu,[a] Xiaosa Li,[a] Jing Guo,[a] Jiajia Shao, [c] Zhong Lin Wang, *[cde] Minyi Xu *[b] and Wenbo Ding *[af]

Triboelectric nanogenerators (TENGs) have demonstrated remarkable capabilities in energy harvesting and self-powered sensing, while TENG theories have set the foundation for their further development. This study presents a systematic theoretical analysis for contact-separation mode TENGs, including theoretical models, analysis methods and validation approaches. Specifically, three infinite plate models are proposed to cover typical forms of contact-separation mode TENGs. According to the physics of charge conservation and electrostatic equilibrium, the distribution of initial charges on tribo-charge layers, and redistribution of all charges on the TENG are determined, based on which the electric field, charge transfer process, conduction current in the external circuit and displacement current inside TENGs are mathematically deduced. TENGs' characteristics and figure of merit can be directly obtained from the proposed theory, which are consistent with phenomena in practice. This validates the theoretical derivations, and better explains TENG performances in practice. Furthermore, applicability is discussed by comparing the finite plate models and infinite plate models, and more accurate schematic diagrams depicting the working principle of TENGs are created. Additionally, an electrodynamic model with a solving approach is proposed that can be applied for TENGs of any size. Extended analysis for different applications is performed, demonstrating the practicability of the proposed theory for TENGs. This work may provide a solid and practical theoretical foundation for TENG development.

Broader context

Basic theories including rigorous theoretical derivations and precise analysis methodologies have set important foundations for the development of TENGs. However, the theoretical framework is still incomplete with limited practical parameters, non-intuitive analysis processes, and lack of effective validation. This study presents a systematic theoretical analysis with solid mathematical derivations for contact-separation mode TENGs. Using the essential variables of initial source charges, theoretical models for different types of TENGs are created. Charge distribution/redistribution (not random but restrained by initial source charges) and the charge transfer process are explained by the mechanism, and equations are deduced step by step rigorously according to basic physical theorems. TENGs' characteristics can be directly obtained from the proposed theory, providing a theoretical prediction/explanation for practical phenomena. This study could be part of a rigorous, applicable and extensible theoretical foundation for TENGs.

[a] Tsinghua-Berkeley Shenzhen Institute, Shenzhen International Graduate School, Tsinghua University, Shenzhen 518055, China.
E-mail: dingwenbo@sz.tsinghua.edu.cn
[b] Marine Engineering College, Dalian Maritime University, Dalian 116026, China.
E-mail: xuminyi@dlmu.edu.cn
[c] Beijing Institute of Nanoenergy and Nanosystems, Chinese Academy of Sciences, Beijing 100085, China. E-mail: zhong.wang@mse.gatech.edu
[d] School of Materials Science and Engineering, Georgia Institute of Technology, Atlanta, GA 30332-0245, USA
[e] Yonsei Frontier Lab, Yonsei University, Seoul 03722, Republic of Korea
[f] RISC-V International Open Source Laboratory, Shenzhen 518055, China
† Electronic supplementary information (ESI) available. See DOI: https://doi.org/10.1039/d3ee04143c
‡ These authors contributed equally: Hongfa Zhao and Hao Wang.

Introduction

As an emerging technology for converting mechanical motions into electricity, triboelectric nanogenerators (TENGs) have demonstrated great potential in energy harvesting and self-powered sensing.[1–5] With significant advantages in terms of cost efficiency, fabrication easiness and material availability, TENGs have been developed for extensive applications such as in environmental energy utilization,[6–9] wearable electronics,[10–13] human–machine interactions,[14–16] and communication.[17–19]

As in most subjects, rigorous theoretical derivations and precise analysis methodologies are the foundation for TENG

design/optimization.[20,21] Proposed in 2012, theoretical models of TENGs have been continuously improved, especially for the most typical contact-separation (CS) mode TENGs.[22–31] The most noteworthy theoretical benchmark includes the capacitance (CA) model proposed in 2013,[32] in which the TENG is treated as an infinite large capacitance model governed by the Gaussian electric field law; the distance-dependent electric field (DDEF) model and the finite-sized charged plane (FSCP) model proposed in 2017,[33,34] in which the TENG consists of finite large plates that can be solved with electrodynamic methods; and the quasi-electrostatic three-dimensional (QETD) model proposed in 2023,[35] in which the electric field distribution can be solved using finite element simulation. However, the theoretical framework is still incomplete with limited practical parameters, non-intuitive analysis processes, and lack of effective validation.

In previous studies, a common assumption is that charge distribution occurs, yet the charge transfer process and the mechanism for charge distribution/redistribution have not been addressed explicitly. This is inadequate for theoretical analysis, as knowledge of charge distribution (the source, on the right-hand side of Maxwell's equations) is a prerequisite for solving the electric field (on the left-hand side of Maxwell's equations). Therefore, more accurate charge distribution, more clear process description, and more rigorous mathematical derivation are what TENGs need within the theoretical dimensions. They would enable accurate solution of both the displacement current (within the TENG) and the conduction current (in the external circuit). Correlating the predictions (for TENG performances) with previous models is common in examining the accuracy of a new model. This is acceptable but not rigorous, as the predictions are based upon multiple input parameters containing inevitable estimation errors. These are the most significant problems lying in TENGs' theory that have not been addressed yet. In addition, the conditions applicable for the infinite plate model and the finite plate model have not been clarified.

In this study, a systematic theoretical analysis for contact-separation mode TENGs is presented, which includes the theoretical models, the analysis methods, validation approaches and application analysis. In particular, the study takes into account the initial charging from contact electrification (CE), pre-charging of the dielectric material, and compensation charging on the base electrode simultaneously for the first time, and proposes self-consistent theoretical models that are more practical for TENG devices. According to the physics of charge conservation and electrostatic equilibrium, the distribution of initial charges and redistribution of all charges, in both the open circuit and connected circuit of the TENG, are revealed. On top of it, the distribution of the electric field, the charge transfer process, the conduction current in the external circuit and the displacement current inside the TENG are derived rigorously. To validate the model, the "predicted characteristics correlating" method is proposed. The solution of TENGs' characteristics and the figure of merit are consistent with the results from the literature, providing a theoretical explanation for the practical phenomena. By comparing the finite plate model with the infinite plate model, their applicable range is discussed. Subsequently, a set of more accurate schematic diagrams for the working principle of TENGs could be depicted. An electrodynamic model along with the solving approach is proposed, so that it can be applied in TENGs of any size. Finally, various applications based on the proposed theory are discussed, providing paradigm for TENGs in practice. This study is the most practical theory for contact-separation mode TENGs at present and is expected to provide a rigorous theoretical foundation for the TENG development.

Results

Theoretical framework

The contact-separation mode TENG, which usually consists of a charged dielectric material with a base electrode, a metal layer serving as both the triboelectric charge layer and independent electrode, a spacer that separates the two layers with a certain distance, and other substrates or protective layers (Fig. 1(a)), is the most common TENG configuration. For the conductor-to-dielectric CS mode TENG, which is commonly used in practice, the typical dielectric materials like polytetrafluoroethylene (PTFE) and fluorinated ethylene propylene (FEP) usually acquire negative charges through contact electrification with other conductive materials. The conductive electrode, on the other hand, often becomes positively charged due to the CE, in which positive and negative charges are redistributed to achieve electrostatic equilibrium (Fig. 1(b), more detailed
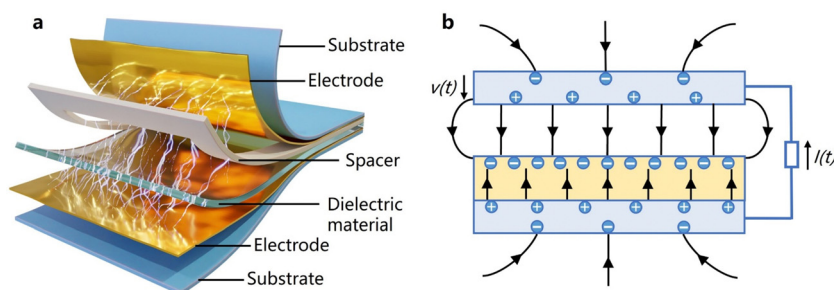

Fig. 1 Schematic diagram of the contact–separation mode TENG. (a) General structure of the TENG. (b) Distribution of charges and the electric field for the TENG.

explanation is provided in Note S1, ESI†). As a result, the total electric field intensity inside the electrode remains zero under the net influences from all charges (including those on the dielectric material as well as external charges). The resultant electric field vector at any point in space is the superposition of the electric fields generated by these charges. As such, the electric field in space is generally curved and both the magnitude and the direction of the electric field vary with coordinates. Under the influence of external forces, the TENG is forced to move/deform, resulting in a varying distance between the dielectric material and the electrode. This leads to variations of the electric field within space, which drives the charge to flow from the electrodes. In the open circuit, charge redistribution occurs on both electrodes. When the two electrodes are connected (either through a short circuit or resistance), the current is generated in the external circuit.

The calculation of charge and electric field distributions mentioned above is based on the electrodynamic methods, which is computationally intensive. Therefore, this approach is not practical in optimizing TENGs. Alternatively, when the size of the TENG significantly exceeds its internal gap, as commonly utilized in the highly sensitive energy harvesters or sensors, a uniform electric field can be approximated inside the TENG. By utilizing the proposed infinite plate model to analyze the charge and electric field distribution, calculations can be significantly simplified while maintaining sufficient accuracy (will be shown in the following sections). Therefore, it is more suitable for optimizing TENG design in practice.

The outline of the study is shown in Fig. 2 and all the different models proposed in this study (including their detailed information, assumptions and limitations) are listed in Table S1 (ESI†). Starting from the basic infinite plate models, the charge distribution of both the dielectric material and the independent electrode resulting from CE is illustrated more precisely. Two types of TENGs are compared: one is formed by a dielectric material and an independent electrode (to generate charge through CE), while the other type is formed by pre-charging the dielectric material with reserve charge *via* CE. The analysis for the general model has taken into account both types of charges mentioned above and the compensation charge on the base electrode (obtained from external materials). The

distribution of charges and electric field under both open and connected states of the TENG and the charge transfer process (varying with the internal distance), are analyzed in detail. In particular, the "predicted characteristics correlating" method is proposed, which is to compare the characteristics (usually non-intuitive) of the TENG with those derived from models and their solutions. If the calculation results match the actual phenomenon, the proposed theoretical model and the analyzing method can be validated. The validity of this model is demonstrated by applications on transforming the contact-separation mode TENG into the single-electrode (SE) mode TENG,[19] as well as in deriving the *V–Q* curve and the figure of merit.[36] Furthermore, the accuracy and applicability range of the infinite plate model is discussed, and an electrodynamics-based analysis method is proposed to accurately determine the charge and electric field distribution for TENGs of any size.

Basic models for the tribo-charge layers

As mentioned above, the dielectric material and the independent electrode acquire opposite charges (of equivalent amount) in the CE, thus they can be described by the classic capacitance model (Fig. 3(ai)) as follows:

$$V = \frac{Q}{C} = \frac{Qz_0}{\varepsilon_0 S} = \frac{\sigma_t z_0}{\varepsilon_0} \qquad (1)$$

$$E = \frac{V}{z_0} = \frac{Q}{\varepsilon_0 S} = \frac{\sigma_t}{\varepsilon_0} \qquad (2)$$

where V, Q, C, E, and S are the potential, the charge, the capacitance, the electric field intensity and the surface area, respectively. z_0 is the distance between the two materials, ε_0 is the vacuum permittivity, and σ_t is the initial charge density on the dielectric material. A uniform electric field is formed between the two materials, and its intensity is independent of the distance. However, the potential difference between the two materials increases proportionally with their distance, while the electric field intensity at other positions is zero. This is consistent with the simulation (simulation approaches for all models are shown in the Experimental section) under the same charge distribution (Fig. 3(b)), and more simulation results are addressed in Note S2 (ESI†). If the independent electrode is
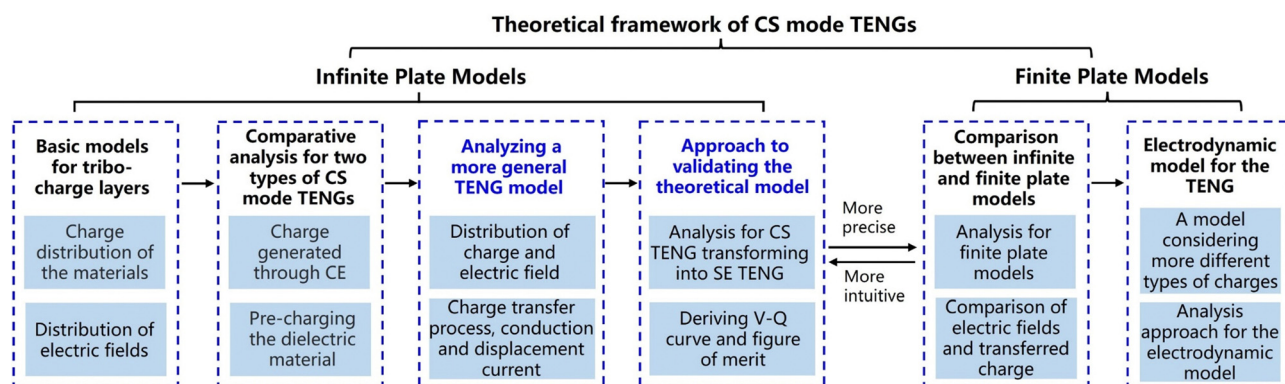

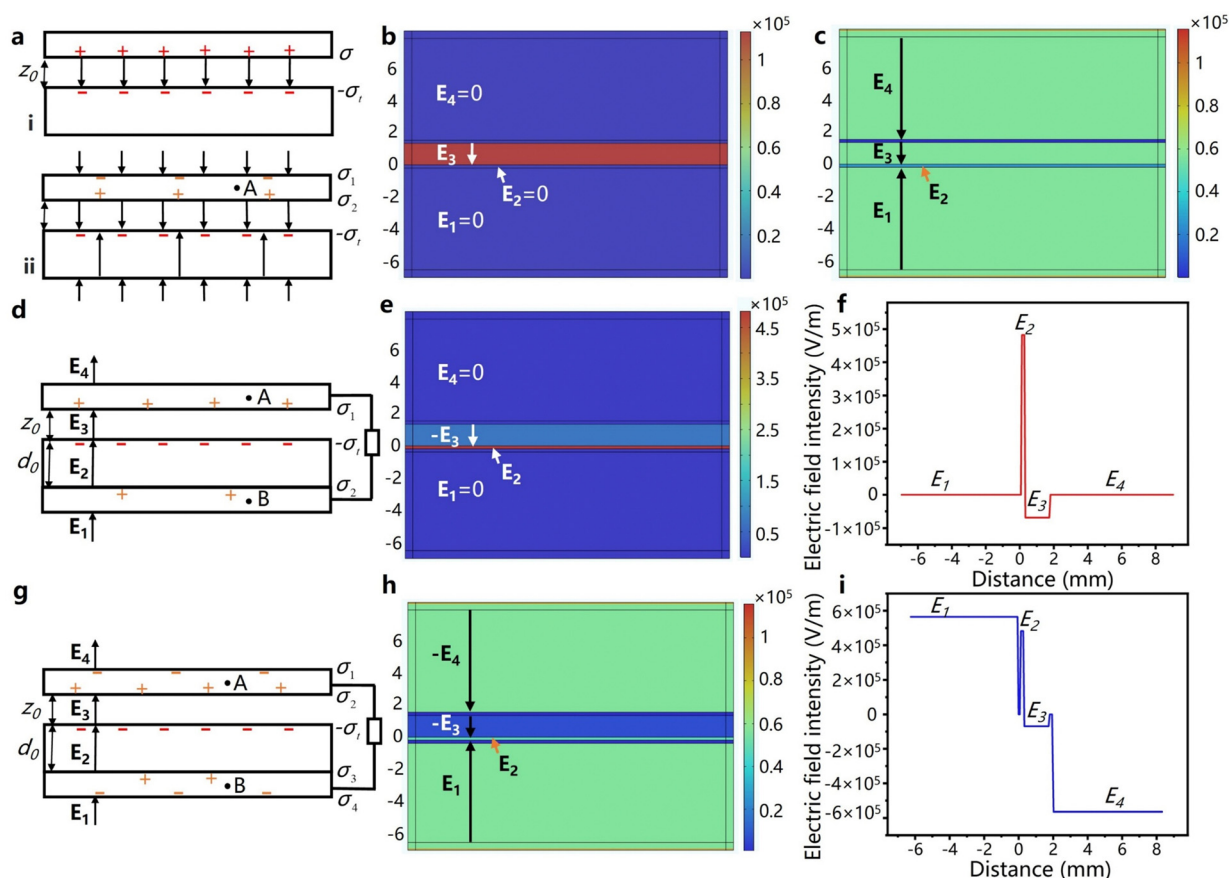**Fig. 2** Theoretical framework of the contact-separation mode TENG.

Fig. 3 Distribution of charges and the electric field for TENG basic models. (a) Schematic diagram of the models for the tribo-charge layers. Simulation of the electric field distribution for (b) the first model and (c) the second model. (d) The TENG model with the tribo-charge layers from the first case. (e) Distribution of the electric field and (f) variation of the electric field intensity with distance for the first type of TENG model. (g) The TENG model with the tribo-charge layers from the second case. (h) Distribution of the electric field and (i) variation of the electric field intensity with distance for the second type of TENG model. At the upper surface of the dielectric material, distance = 0, and E_2 represents the electric field intensity inside the dielectric material.

grounded and a resistance is connected in the external circuit, a single-electrode TENG model is formed. The infinite plate model can only return its voltage theoretically, while the transferred charges and the current should be obtained with electrodynamic approaches (the details are shown in Note S3, ESI†). For the same reason, the TENG models with two tribo-charge layers should be analyzed with electrodynamic approaches as the leakage field at the edge need be considered for the output of the TENG.[22,37]

Common dielectric materials, such as polytetrafluoroethylene (PTFE) and fluorinated ethylene propylene (FEP), possess strong electronegativity and tend to accumulate charges through the CE.[38–40] Pre-charging is considered as a viable approach for enhancing the TENG performance. In this case, the TENG model is different from the first one (Fig. 3(aii) and (c)). The electric field distribution is no longer confined between the two materials. The electrode separates equal (but opposite) charges on the upper and bottom surface so that an electrostatic equilibrium is reached. However, when connected to a resistance and grounded to fabricate a single-electrode TENG, the charge distribution will be the same as the first model (detailed analysis is provided in Note S4, ESI†).

Comparative analysis for two types of CS mode TENGs

Two types of tribo-charge layers have been discussed above. For the first case, the corresponding TENG model is shown in Fig. 3(d) (its open-circuit model is shown in Note S5, ESI†). The two electrodes are connected by an external circuit, so their potentials will be equal at equilibrium. At any point inside the electrodes, the electric field intensity is zero. The potential at the upper surface of the dielectric material is defined as V_t, and the upward direction is defined as positive direction of the electric field. Consequently, the following two equations can be derived:

$$\begin{cases} -\dfrac{\sigma_t}{2\varepsilon_0} + \dfrac{\sigma_1}{2\varepsilon_0} + \dfrac{\sigma_2}{2\varepsilon_0} = 0 \\[2mm] V_t - \left(-\dfrac{\sigma_t}{2\varepsilon_0} - \dfrac{\sigma_1}{2\varepsilon_0} + \dfrac{\sigma_2}{2\varepsilon_0} \right)z_0 = V_t + \left(\dfrac{\sigma_t}{2\varepsilon_0\varepsilon_r} - \dfrac{\sigma_1}{2\varepsilon_0\varepsilon_r} + \dfrac{\sigma_2}{2\varepsilon_0\varepsilon_r} \right)d_0 \end{cases}$$

$$(3)$$

where σ_1 and σ_2 are the charge on the two electrodes, respectively. ε_r is the relative permittivity, and d_0 is the thickness of the dielectric material. The two unknown quantities can be

determined by solving the following equations:

$$
\begin{cases}
\sigma_1 = \dfrac{\sigma_t d_0}{\varepsilon_r z_0 + d_0} \\[3mm]
\sigma_2 = \dfrac{\sigma_t \varepsilon_r z_0}{\varepsilon_r z_0 + d_0}
\end{cases}
\tag{4}
$$

The distribution of the electric field in the space can be calculated as:

$$
\mathbf{E_1} = \mathbf{E_4} = 0 \tag{5}
$$

$$
\mathbf{E_2} = \left(\frac{\sigma_t}{2\varepsilon_0 \varepsilon_r} - \frac{\sigma_1}{2\varepsilon_0 \varepsilon_r} + \frac{\sigma_2}{2\varepsilon_0 \varepsilon_r} \right) \mathbf{e_z} = \frac{\sigma_t z_0 \mathbf{e_z}}{\varepsilon_0 (\varepsilon_r z_0 + d_0)} \tag{6}
$$

$$
\mathbf{E_3} = \left(-\frac{\sigma_t}{2\varepsilon_0} - \frac{\sigma_1}{2\varepsilon_0} + \frac{\sigma_2}{2\varepsilon_0} \right) \mathbf{e_z} = \frac{-\sigma_t z_0 \mathbf{e_z}}{\varepsilon_0 (\varepsilon_r z_0 + d_0)} \tag{7}
$$

where $\mathbf{e_z}$ is the unit vector pointing upward. To examine the derivation, reasonable values are substituted into each parameter to calculate the charge on both electrodes. Then the parameters (including the charge on electrodes) are input into the finite element simulation. The electric field distribution from the simulation is compared with the analytical solution. It is assumed that $z_0 = 1.4$ mm, $d_0 = 0.2$ mm, $\sigma_t = 10^{-5}$ C m^{-2}, $\varepsilon_r = 2.2$, and the charge on two electrodes is $\sigma_1 = 5\sigma_t/82$ and $\sigma_2 = 77\sigma_t/82$. The simulation results with these parameters are shown in Fig. 3(e) and (f), which are consistent with the results calculated from eqn (5)–(7): $E_1 = E_4 = 0$, $E_2 = 4.82 \times 10^5$ V m^{-1}, $E_3 = -6.89 \times 10^4$ V m^{-1}. Similarly, the simulated potential distribution also shows consistency with that from the analytical solution, as detailed in Note S6 (ESI†).

For the second type TENG (corresponding to the second model of tribo-charge layers in Fig. 3(aii)), the open-circuit TENG model is solved and validated in Note S7 (ESI†). When its two electrodes are connected by a resistance, the physical model is depicted in Fig. 3(g). To fulfill charge conservation, the zero electric field in the electrodes, and equal potential on both electrodes, the governing equations can be written as:

$$
\begin{cases}
-\sigma_1 + \sigma_2 + \sigma_3 - \sigma_4 = 0 \\[2mm]
-\dfrac{\sigma_t}{2\varepsilon_0} + \dfrac{\sigma_1}{2\varepsilon_0} + \dfrac{\sigma_2}{2\varepsilon_0} + \dfrac{\sigma_3}{2\varepsilon_0} - \dfrac{\sigma_4}{2\varepsilon_0} = 0 \\[2mm]
\dfrac{\sigma_t}{2\varepsilon_0} + \dfrac{\sigma_1}{2\varepsilon_0} - \dfrac{\sigma_2}{2\varepsilon_0} - \dfrac{\sigma_3}{2\varepsilon_0} - \dfrac{\sigma_4}{2\varepsilon_0} = 0 \\[2mm]
V_t - \left(-\dfrac{\sigma_t}{2\varepsilon_0} + \dfrac{\sigma_1}{2\varepsilon_0} - \dfrac{\sigma_2}{2\varepsilon_0} + \dfrac{\sigma_3}{2\varepsilon_0} - \dfrac{\sigma_4}{2\varepsilon_0} \right) z_0 = V_t + \left(\dfrac{\sigma_t}{2\varepsilon_0 \varepsilon_r} + \dfrac{\sigma_1}{2\varepsilon_0 \varepsilon_r} - \dfrac{\sigma_2}{2\varepsilon_0 \varepsilon_r} + \dfrac{\sigma_3}{2\varepsilon_0 \varepsilon_r} - \dfrac{\sigma_4}{2\varepsilon_0 \varepsilon_r} \right) d_0
\end{cases}
\tag{8}
$$

where σ_1, σ_2, σ_3, and σ_4 are the charge density on the four surfaces of the two electrodes, respectively. The solutions are as follows:

$$
\begin{cases}
\sigma_1 = \sigma_4 = \dfrac{\sigma_t}{2} \\[2mm]
\sigma_2 = \dfrac{\sigma_t d_0}{z_0 \varepsilon_r + d_0} \\[2mm]
\sigma_3 = \dfrac{\sigma_t z_0 \varepsilon_r}{z_0 \varepsilon_r + d_0}
\end{cases}
\tag{9}
$$

The distribution of the electric field is:

$$
\mathbf{E_1} = \frac{\sigma_t}{2\varepsilon_0} \mathbf{e_z} \tag{10}
$$

$$
\mathbf{E_2} = \left(\frac{\sigma_t}{2\varepsilon_0 \varepsilon_r} + \frac{\sigma_1}{2\varepsilon_0 \varepsilon_r} - \frac{\sigma_2}{2\varepsilon_0 \varepsilon_r} + \frac{\sigma_3}{2\varepsilon_0 \varepsilon_r} - \frac{\sigma_4}{2\varepsilon_0 \varepsilon_r} \right) \mathbf{e_z} = \frac{\sigma_t z_0}{\varepsilon_0 (z_0 \varepsilon_r + d_0)} \mathbf{e_z} \tag{11}
$$

$$
\mathbf{E_3} = \left(-\frac{\sigma_t}{2\varepsilon_0} + \frac{\sigma_1}{2\varepsilon_0} - \frac{\sigma_2}{2\varepsilon_0} + \frac{\sigma_3}{2\varepsilon_0} - \frac{\sigma_4}{2\varepsilon_0} \right) \mathbf{e_z} = -\frac{\sigma_t d_0}{\varepsilon_0 (z_0 \varepsilon_r + d_0)} \mathbf{e_z} \tag{12}
$$

By substituting the same set of parameters adopted in the first type TENG into eqn (9), the charge distribution is obtained. These parameters are then taken into the finite element simulation, which returns the results shown in Fig. 3(h)–(i). The simulated electric field distribution is also consistent with the analytical solution. It is clear that in this model, charge transfer takes place between the two electrodes of the TENG, resulting in a net charge on each electrode (positive and negative charges are separated on each electrode), maintaining an electrostatic equilibrium.

The two types of models analyzed above represent the common approaches of initializing TENGs, while the former has a stronger internal electric field, giving rise to higher open-circuit voltage. When the two TENGs are of the same structure and dimensions, the net charge difference between their two electrodes is the same (equivalent amount of charge will be transferred in both TENGs under identical motion). As the distance between the dielectric material and upper electrode increases, the transferred charge is:

$$
\frac{\sigma_t (\varepsilon_r (z + \Delta z) - d_0)}{2(\varepsilon_r (z + \Delta z) + d_0)} - \frac{\sigma_t (\varepsilon_r z - d_0)}{2(\varepsilon_r z + d_0)} = \frac{\sigma_t \varepsilon_r \Delta z d_0}{2(\varepsilon_r z + d_0)(\varepsilon_r (z + \Delta z) + d_0)}
\tag{13}
$$

Different approaches should be considered in fabricating different TENGs.

Analyzing a more general TENG model

So far, two types of TENG models have been analyzed. Earlier TENG modeling studies have been mostly based on models similar to the first type (and the comparisons are shown in Table S2, ESI†). However, the second type, which involves pre-charging of the dielectric material as an approach for enhancing the TENG performance, is also analyzed in this study. However, actual charge distribution is more complex. Previous

studies by Prof. Wang have revealed that bias voltage can significantly affect the ability of a material to gain/lose electrons.[41] It means the base electrode can easily acquire positive charges under the influence of a negatively charged dielectric material with a strong electrostatic field. As a result, it may be inevitable for the base electrode to accumulate positive charges when in contact with other substances (such as human skin).

To cover all types of charges, including the pre-charging charges σ_t, the positive compensation charges acquired by the base electrode σ_c, the contact-electrification charges σ'_t, and the positive and negative charges separated by electrodes to achieve electrostatic equilibrium σ_1, σ_2, σ_3, and σ_4 (Fig. 4(a), three initial charge distribution and four induced charge distribution), a more general TENG model is analyzed. The simulated electric field distribution for the open-circuit model (Fig. 4(aii)) is shown in Fig. 4(b) and (c), corresponding to the solution detailed in Note S8 (ESI†), and its open-circuit voltage can be derived as:

$$V = \frac{(\sigma_t + \sigma_c)d_0 + (\sigma_t - \sigma_c + 2\sigma'_t)\varepsilon_r z_0}{2\varepsilon_0\varepsilon_r} \quad (14)$$

The model with two electrodes connected *via* a resistance is shown in Fig. 4(aiii). To fulfill charge conservation, electrostatic equilibrium, and equipotentiality of the electrodes, a set of equations have been derived:

$$\begin{cases} -\sigma_1 + \sigma_2 + \sigma_3 - \sigma_4 = \sigma'_t + \sigma_c \\ -\frac{\sigma_t + \sigma'_t}{2\varepsilon_0} + \frac{\sigma_1}{2\varepsilon_0} + \frac{\sigma_2}{2\varepsilon_0} + \frac{\sigma_3}{2\varepsilon_0} - \frac{\sigma_4}{2\varepsilon_0} = 0 \\ \frac{\sigma_t + \sigma'_t}{2\varepsilon_0} + \frac{\sigma_1}{2\varepsilon_0} - \frac{\sigma_2}{2\varepsilon_0} - \frac{\sigma_3}{2\varepsilon_0} - \frac{\sigma_4}{2\varepsilon_0} = 0 \\ V_t - \left(-\frac{\sigma_t + \sigma'_t}{2\varepsilon_0} + \frac{\sigma_1}{2\varepsilon_0} - \frac{\sigma_2}{2\varepsilon_0} + \frac{\sigma_3}{2\varepsilon_0} - \frac{\sigma_4}{2\varepsilon_0}\right)z_0 = V_t + \left(\frac{\sigma_t + \sigma'_t}{2\varepsilon_0\varepsilon_r} + \frac{\sigma_1}{2\varepsilon_0\varepsilon_r} - \frac{\sigma_2}{2\varepsilon_0\varepsilon_r} + \frac{\sigma_3}{2\varepsilon_0\varepsilon_r} - \frac{\sigma_4}{2\varepsilon_0\varepsilon_r}\right)d_0 \end{cases} \quad (15)$$

The corresponding solutions are:

$$\begin{cases} \sigma_1 = \frac{\sigma_t - \sigma_c}{2} \\ \sigma_2 = \frac{(\sigma_t + \sigma'_t)d_0}{z_0\varepsilon_r + d_0} \\ \sigma_3 = \frac{(\sigma_t + \sigma'_t)z_0\varepsilon_r}{z_0\varepsilon_r + d_0} \\ \sigma_4 = \frac{\sigma_t - \sigma_c}{2} \end{cases} \quad (16)$$

The corresponding electric fields are:

$$\mathbf{E}_1 = \frac{\sigma_t - \sigma_c}{2\varepsilon_0}\mathbf{e_z} \quad (17)$$

$$\mathbf{E}_2 = \left(\frac{\sigma_t + \sigma'_t}{2\varepsilon_0\varepsilon_r} + \frac{\sigma_1}{2\varepsilon_0\varepsilon_r} - \frac{\sigma_2}{2\varepsilon_0\varepsilon_r} + \frac{\sigma_3}{2\varepsilon_0\varepsilon_r} - \frac{\sigma_4}{2\varepsilon_0\varepsilon_r}\right)\mathbf{e_z} = \frac{(\sigma_t + \sigma'_t)z_0}{\varepsilon_0(z_0\varepsilon_r + d_0)}\mathbf{e_z} \quad (18)$$

$$\mathbf{E}_3 = \left(-\frac{\sigma_t + \sigma'_t}{2\varepsilon_0} + \frac{\sigma_1}{2\varepsilon_0} - \frac{\sigma_2}{2\varepsilon_0} + \frac{\sigma_3}{2\varepsilon_0} - \frac{\sigma_4}{2\varepsilon_0}\right)\mathbf{e_z} = -\frac{(\sigma_t + \sigma'_t)d_0}{\varepsilon_0(z_0\varepsilon_r + d_0)}\mathbf{e_z} \quad (19)$$

$$\mathbf{E}_4 = \frac{\sigma_c - \sigma_t}{2\varepsilon_0}\mathbf{e_z} \quad (20)$$

By substituting the values in Note S8 (ESI†) into each parameter, the electric field distribution can be calculated: $E_1 = 2.26 \times 10^5$ V m^{-1}, $E_2 = 4.82 \times 10^5$ V m^{-1}, $E_3 = -0.69 \times 10^5$ V m^{-1}, and $E_4 = -2.26 \times 10^5$ V m^{-1}. The corresponding numerical simulation results for the electric field distribution are depicted in Fig. 4(d) and (e), in which the electric fields inside the electrodes are zero, the two electrodes have equal potential ($E_2d_0 + E_3z_0 = 0$ according to the data in Fig. 4e), and the electric fields in the space are all equal to those calculated using the equations, so the simulation results prove that the calculation process is correct (more details for the numerical simulations are shown in the Experimental section). Therefore, the charge distribution on the two electrodes, the spatial electric field distribution and the potential difference between any two points of the TENG can be solved analytically under either open-circuit or a connected state, given the source charge, the material thickness, and internal distance of the TENG.

Eqn (16) reveals that it is possible to have a net positive charge, a net negative charge, or a net zero charge on the two electrodes, and the difference in net charge between the two electrodes is:

$$q(z) = [\sigma_3 - \sigma_4 - (\sigma_2 - \sigma_1)]S = \frac{(\sigma_t + \sigma'_t)(z\varepsilon_r - d_0)S}{z\varepsilon_r + d_0} \quad (21)$$

When the distance between the dielectric material and the independent electrode increases by dz, the corresponding transferred charge is:

$$\mathrm{d}Q = \frac{1}{2}[q(z + \mathrm{d}z) - q(z)] \quad (22)$$

The equation can be converted into the following form:

$$\frac{\mathrm{d}Q}{\mathrm{d}z} = \frac{1}{2}\frac{q(z + \mathrm{d}z) - q(z)}{\mathrm{d}z} = \frac{1}{2}\frac{\mathrm{d}q}{\mathrm{d}z} = \frac{(\sigma_t + \sigma'_t)\varepsilon_r S d_0}{(z\varepsilon_r + d_0)^2} \quad (23)$$
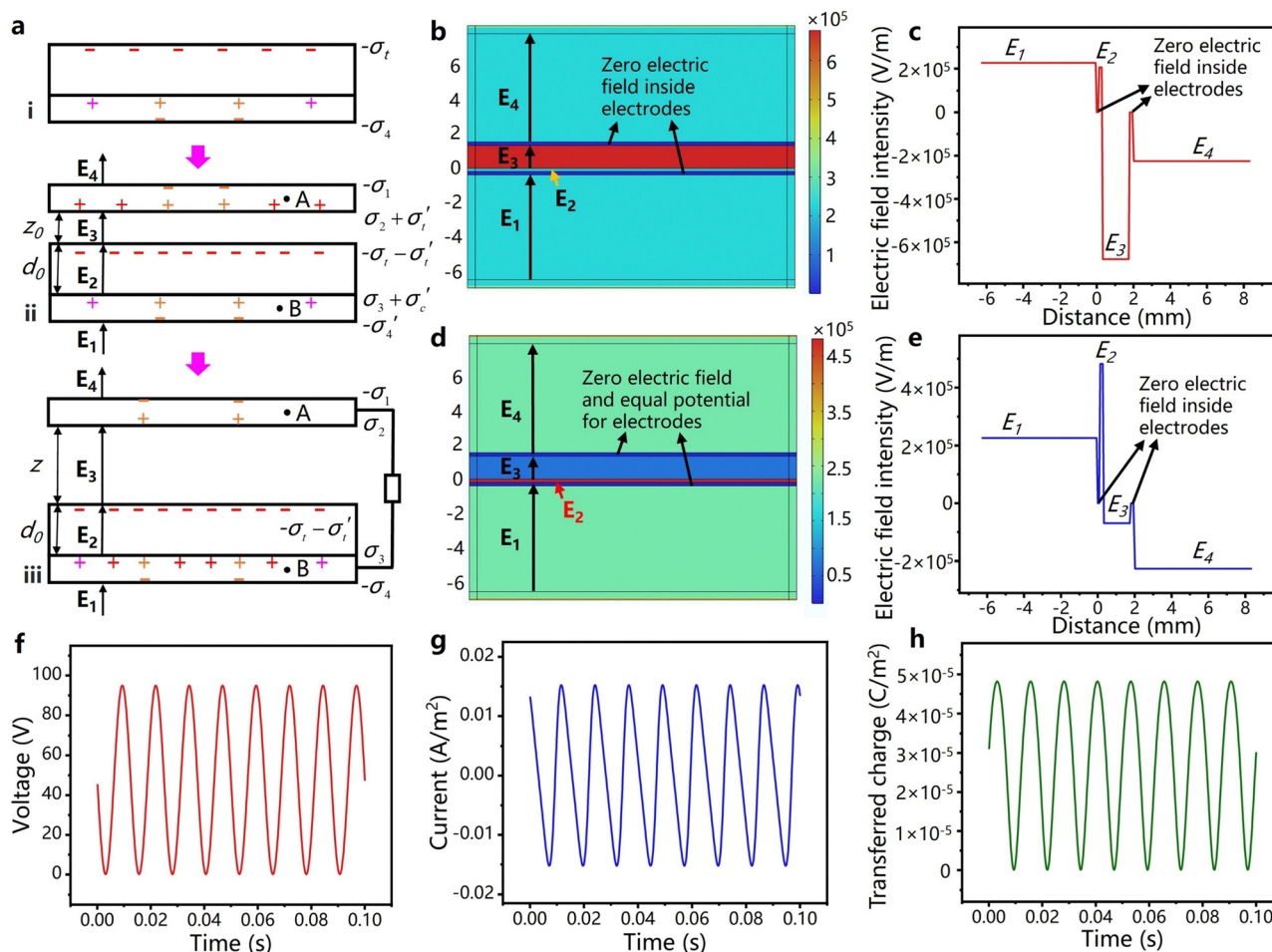
Fig. 4 Calculation and simulation results for the general model. (a) Schematic diagram of the model in different states. (b) Distribution of the electric field and (c) variation of the electric field intensity for the model in (aii). (d) Distribution of the electric field and (e) variation of the electric field intensity for the model in (aiii). (f) Theoretical voltage, (g) theoretical current density and (h) theoretical charge density for a contact–separation mode TENG.

The relationship between the transferred charge and the distance z is:

$$Q = \int_{z_1}^{z_2} \mathrm{d}Q = \int_{z_1}^{z_2} \frac{\left(\sigma_t + \sigma_t'\right)\varepsilon_r S d_0}{\left(z\varepsilon_r + d_0\right)^2}\mathrm{d}z$$

$$= \left(\sigma_t + \sigma_t'\right)\varepsilon_r S d_0 \int_{z_1}^{z_2} \frac{\mathrm{d}z}{\left(z\varepsilon_r + d_0\right)^2} = \frac{\left(\sigma_t + \sigma_t'\right)\varepsilon_r S d_0(z_2 - z_1)}{(z_1\varepsilon_r + d_0)(z_2\varepsilon_r + d_0)}$$

(24)

If the time increment is $\mathrm{d}t$ and the transferred charge is $\mathrm{d}q$, then the current is:

$$I(t) = \frac{\mathrm{d}Q}{\mathrm{d}t} = \frac{\mathrm{d}Q}{\mathrm{d}z}v = \frac{\left(\sigma_t + \sigma_t'\right)\varepsilon_r S d_0 v}{\left(z\varepsilon_r + d_0\right)^2}$$

(25)

It can be found that the current correlates positively with velocity v, which is consistent with the experimental results from many studies.[42–45] From eqn (19), the displacement current density can be derived:

$$\frac{\partial D}{\partial t} = \varepsilon_0\frac{\partial E_3}{\partial t} = \varepsilon_0\frac{\partial E_b}{\partial z}\frac{\partial z}{\partial t} = \frac{\left(\sigma_t + \sigma_t'\right)d_0\varepsilon_r v}{\left(z\varepsilon_r + d_0\right)^2}$$

(26)

where D is the electric flux density, so the displacement current inside the TENG is:

$$I_d = \int_S \frac{\partial D}{\partial t}\mathrm{d}S = \frac{\left(\sigma_t + \sigma_t'\right)d_0\varepsilon_r S v}{\left(z\varepsilon_r + d_0\right)^2}$$

(27)

Comparing eqn (25) with eqn (27) reveals that the displacement current inside the TENG equals the conduction current in the external circuit. When the TENG comes into contact, the internal distance z of the TENG decreases. According to eqn (16), σ_2 will increase while σ_3 will decrease, and a negative value will be achieved from eqn (24). That means (positive) charge transfer occurs from the base electrode of the dielectric material to the independent electrode. While when the TENG is in the separation process, charge transfer occurs from the independent electrode to the base electrode of the dielectric material (the details are shown in Note S9, ESI†).

The theoretical model and solution for the TENG are derived rigorously, yet achieving accurate results relies on precise knowledge of source charges and TENG motions. Reasonable parameters reflecting charge distribution and motion states (as in a previous study on the acoustic-driven TENG[46]) are provided

as the input to the theoretical model (details of estimated parameters are shown in Note S10, ESI†), and the obtained results are shown in Fig. 4(f)–(h). The open-circuit voltage, the short-circuit current and the transferred charge measured using the electrometer of the acoustic-driven TENG are 94.5 V, 13 μA, and 42 nC, respectively (Note S11, ESI†). The voltage, the current and the transferred charge from analytical solution are 95 V, 13.5 μA, and 43 nC, respectively. The analysis has good agreement with the experiment, while the errors come from the input estimation errors (*i.e.* TENG material charge, internal distance, and actual motions). A more rigorous validation approach is introduced in the following section. In addition, this study mainly focuses on the conductor-to-dielectric CS mode TENGs, but in fact, the proposed approach is quite universal and can also be used to analyze the dielectric-to-dielectric CS mode TENGs (Note S12, ESI†), which are also commonly used in practice.[47]

Approach to validating the theoretical model

The theoretical model is derived from basic physics of TENG devices, and the analysis results should be consistent with the explicit characteristics of the TENG (Fig. 5). Previous studies usually compare the voltage, the current and the transferred charge predictions from a theoretical model with the experimental data, as well as with the predictions from other theoretical models. Those are meaningful but incomplete, as estimated values (rather than true values) are adopted in those predictions, Therefore, an approach of "predicted characteristics correlating" is proposed, which compares the non-intuitive characteristics of the TENG with the theoretical predictions, as shown in Fig. 5. If the predictions match the characteristics

(phenomena) in practice, the proposed theoretical model is validated.

Our previous study indicates that a CS mode TENG can be transformed into a SE mode TENG, with one electrode grounded and the other as the output electrode. The output performance will remain unchanged. The proposed model and analytical approaches are used to analyze why TENGs have these characteristics. In this section, the equations, theoretical results, and experimental data for the CS mode TENG and transformed SE TENG are compared, respectively. The theoretical model for the transformed single-electrode mode TENG is shown in Fig. 6(a) (note that the initial charge distribution on the dielectric material should be the same as the original CS mode TENG, as shown in Fig. 4(a)). Since the electric field inside the electrodes is zero and the potential of the electrodes is zero, the following equations can be derived:

$$
\begin{cases}
-\dfrac{\sigma_t + \sigma_t^{'}}{2\varepsilon_0} + \dfrac{\sigma_2}{2\varepsilon_0} + \dfrac{\sigma_3}{2\varepsilon_0} = 0 \\[2mm]
\dfrac{\sigma_3}{\varepsilon_0 \varepsilon_{\mathrm{r}}} d_0 - \dfrac{\sigma_2}{\varepsilon_0} z_0 = 0
\end{cases}
\tag{28}
$$

The corresponding solution is:

$$
\begin{cases}
\sigma_2 = \dfrac{(\sigma_t + \sigma_t^{'}) d_0}{z_0 \varepsilon_{\mathrm{r}} + d_0} \\[2mm]
\sigma_3 = \dfrac{(\sigma_t + \sigma_t^{'}) z_0 \varepsilon_{\mathrm{r}}}{z_0 \varepsilon_{\mathrm{r}} + d_0}
\end{cases}
\tag{29}
$$

Comparing the results with eqn (16), (18) and (19), the charge distribution and the electric field inside the TENG of the transformed SE TENG are exactly the same as those of CS
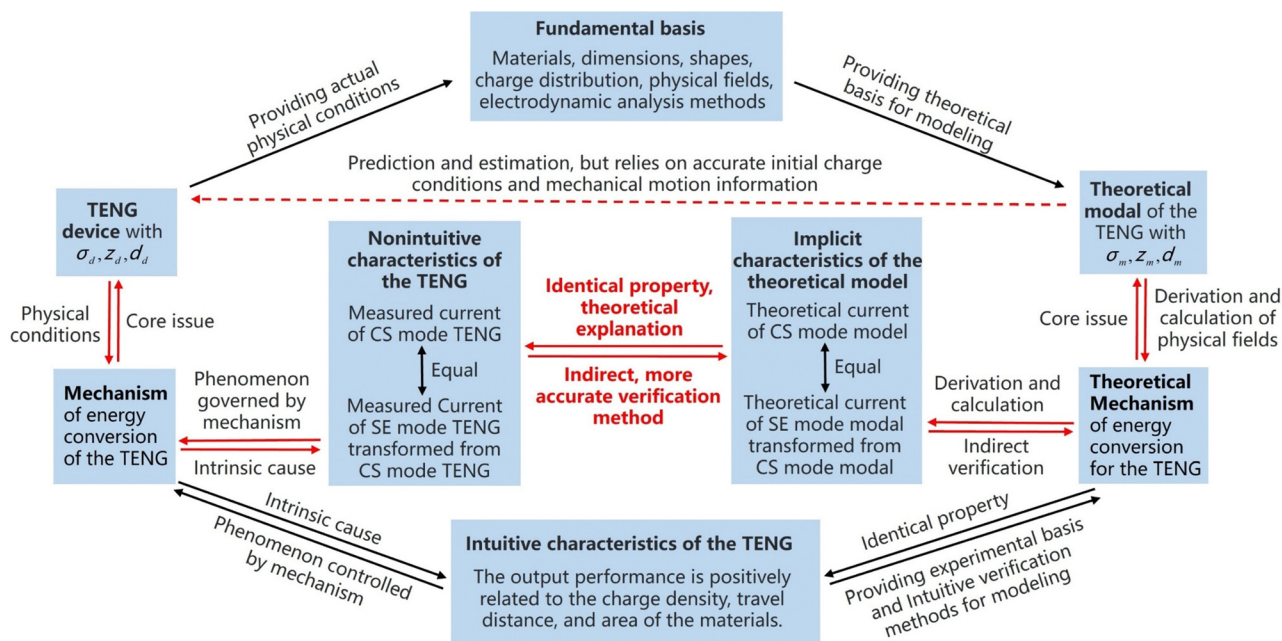

Fig. 5 Framework of the approach for validating the theoretical model.

Energy & Environmental Science

Paper

mode TENG (Fig. 4(aiii)). The corresponding transferred charge on the electrode and the current in the circuit is:

$$Q = \int_{z_1}^{z_2} \mathrm{d}Q = \int_{z_1}^{z_2} \frac{\mathrm{d}\sigma_2}{\mathrm{d}z}\mathrm{d}z = \int_{z_1}^{z_2} \frac{(\sigma_t + \sigma_t')\varepsilon_r S d_0}{(z\varepsilon_r + d_0)^2}\mathrm{d}z$$
$$= \frac{(\sigma_t + \sigma_t')\varepsilon_r S d_0(z_2 - z_1)}{(z_1\varepsilon_r + d_0)(z_2\varepsilon_r + d_0)} \tag{30}$$

$$I(t) = \frac{\mathrm{d}Q}{\mathrm{d}t} = \frac{\mathrm{d}\sigma_2}{\mathrm{d}z}\frac{S}{\mathrm{d}t}\frac{\mathrm{d}z}{\mathrm{d}t} = \frac{(\sigma_t + \sigma_t')\varepsilon_r S d_0 v}{(z\varepsilon_r + d_0)^2} \tag{31}$$

The comparison of eqn (30) and (31) with eqn (24) and (25) shows that mathematically the output performances of the transformed SE TENG are identical to those of the original CS mode TENG. Moreover, the same values (as used in the CS TENG) of the charge density on the dielectric material and the motion states (as in Note S10, ESI†) are used for simulations. The distribution of the electric field is shown in Fig. 6(b) and (c), which is consistent with that from the contact-separation model (in Note S13, ESI†). In the simulation, the charge on the independent electrode induced by the charge on the dielectric material can be calculated (Fig. 6(d)). Subsequently, the transferred charge and current can be obtained based on the simulation data (Fig. 6(e) and (f)), based on the parameters of the acoustic driven TENG. The output parameters of the transformed SE mode TENG from the theoretical results also matches the output parameters from the CS mode TENG (Fig. 4(g) and (h)). As for experiment results, the schematic diagram, transferred charge and current of the original CS mode TENG are shown in Fig. 6(g)–(i), and those of transformed SE mode TENG are shown in Fig. 6j–l. The output performance of the CS mode TENG is nearly the same as that of the transformed SE mode TENG, which is consistent with the theoretical results.

What's more, if the electrode is not grounded, the output current will be significantly reduced to almost zero. If the independent electrode is grounded and the base electrode serves as the outputting electrode, the output performance of the TENG will remain unchanged. The corresponding theoretical model, solution and experimental details are shown in Note S14 and S15 (ESI†), and the explanations for the grounding method are provided in Note S16 (ESI†). All theoretical analysis is consistent with the actual phenomena. It means that the physical model and its corresponding solution have effectively addressed the characteristics (the CS mode TENG transforming into the SE mode TENG) of the TENG.

The figure of merit (FOM, derived from the V–Q curve of the TENG) is proposed by Prof. Zi and has been an important index of evaluating TENGs.[36] The study proposed an approach for the TENG to obtain maximum output energy from the V–Q curve in one working cycle. It defined the structural FOM (FOM_S, dimensionless), performance FOM (FOM_P), and material FOM (FOM_m) using parameters including charge density σ and maximum output energy E_m. In the manuscript, we use mathematical analysis to describe the V–Q curve of the TENG during

the working process, and verify the dimensionless properties of FOM_S with more basic parameters.

Based on the theoretical model and equations above, the V–Q curve and the figure of merit of the TENG can be comprehensively calculated and explained. When the external circuit is open, the TENG is deformed by the external force and no charge transfer occurs. Then the circuit is connected so that the current flows through the resistors and enables maximum energy output in a discharge process. If the initial distance between the dielectric material and the independent electrode is z_1 (the charge distribution is in equilibrium), under the excitation of external forces, the internal distance of the TENG changes to z_2 (during which the external circuit is open), then according to the general TENG model (Fig. 4(a)) the potential difference between the two electrodes changes from zero to:

$$V_0 = -\frac{(\sigma_t + \sigma_t')z_1 d_0}{\varepsilon_0(z_1\varepsilon_r + d_0)} + \frac{(\sigma_t + \sigma_t')d_0 z_2}{\varepsilon_0(z_1\varepsilon_r + d_0)} = \frac{(\sigma_t + \sigma_t')d_0(z_2 - z_1)}{\varepsilon_0(z_1\varepsilon_r + d_0)} \tag{32}$$

After connecting the external circuit, the total charge transferred from the independent electrode to the base electrode is:

$$Q_0 = \frac{(\sigma_t + \sigma_t')\varepsilon_r S d_0(z_2 - z_1)}{(z_1\varepsilon_r + d_0)(z_2\varepsilon_r + d_0)} \tag{33}$$

In the charge transfer process, when there is a charge of q transferred from the independent electrode to the base electrode, the voltage between the two electrodes is:

$$V = -\frac{\left(\sigma_t + \sigma_t' + \frac{q}{S}\right)z_1 d_0}{\varepsilon_0(z_1\varepsilon_r + d_0)} + \frac{\left(\sigma_t + \sigma_t' - \frac{q}{S}\right)d_0 z_2}{\varepsilon_0(z_1\varepsilon_r + d_0)}$$
$$= \frac{(\sigma_t + \sigma_t')d_0(z_2 - z_1)}{\varepsilon_0(z_1\varepsilon_r + d_0)} - \frac{d_0(z_1 + z_2)}{\varepsilon_0(z_1\varepsilon_r + d_0)S}q \tag{34}$$

The correlation between the voltage V and the transferred charge Q is linear, which is consistent with the simulation and experimental results from the literature.[36]

In the first stage, if the two electrodes are connected by a large resistor sufficient to affect the charge transfer process during the change of the internal distance z, the voltage between the two electrodes is:

$$V = \int \left(\frac{(\sigma_t + \sigma_t')d_0}{\varepsilon_0(z\varepsilon_r + d_0)} - \frac{2d_0 z}{\varepsilon_0(z\varepsilon_r + d_0)S}\int \frac{(\sigma_t + \sigma_t')d_0 v\,\mathrm{d}t}{\varepsilon_0(z\varepsilon_r + d_0)R} \right)\mathrm{d}z \tag{35}$$

The derivation process of eqn (35) is shown in Note S17 (ESI†). As the resistance R increases, the second term decreases. As R approaches infinity, only the first term in the equation remains, and eqn (35) will converge to the form of eqn (32). When the distance reaches maximum, connect the two electrodes in short circuit, thus the TENG returns to the discharge process as expressed in eqn (34).
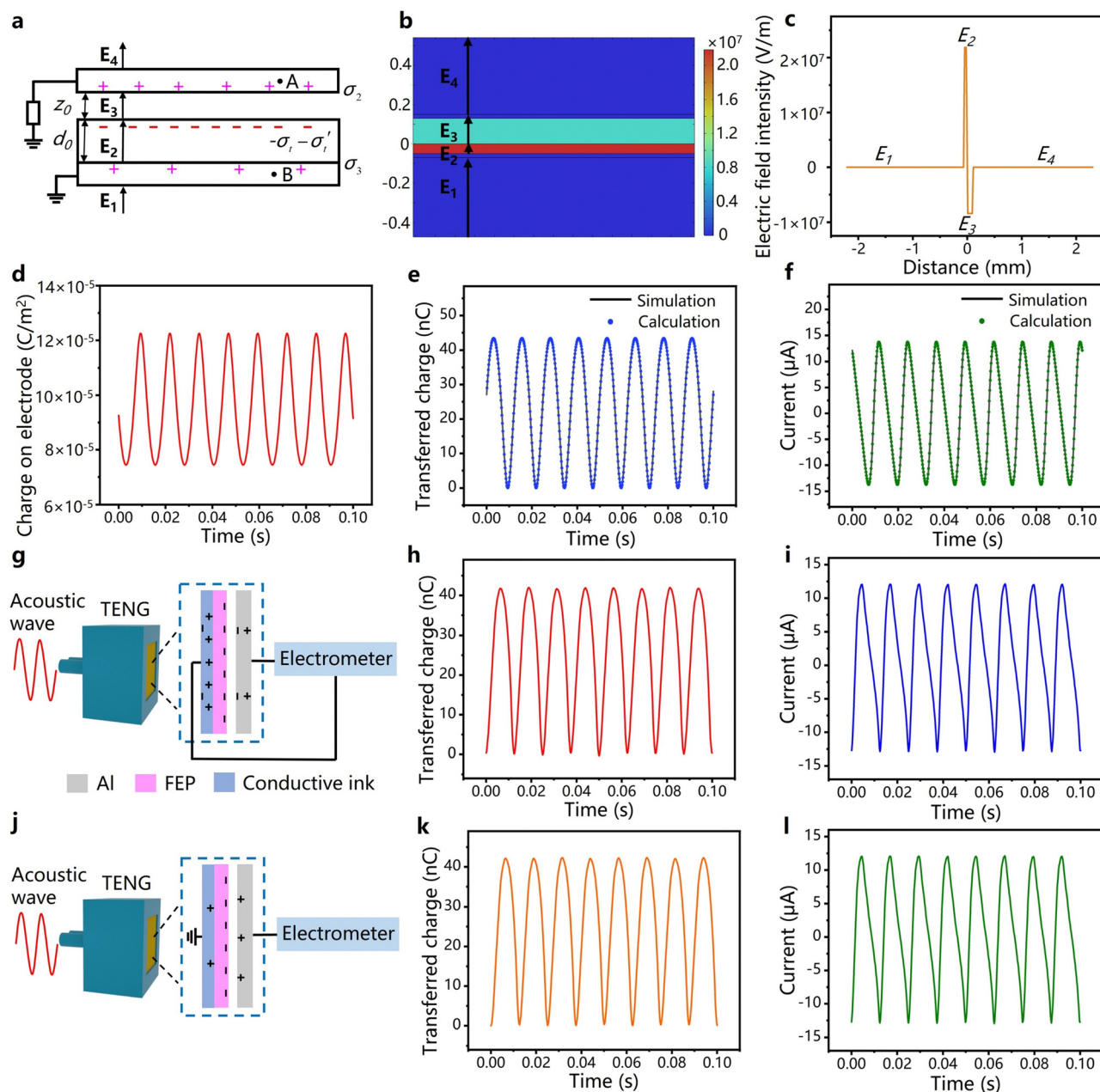
Fig. 6 Analysis of the transformed single-electrode TENG. (a) Schematic diagram of the TENG model. (b) Distribution of the electric field. (c) Variation of the electric field intensity with distance. (d) Charge on the independent electrode derived from simulation. Comparison of simulation and calculation results for (e) transferred charge and (f) current (derived based on the parameters of the acoustic driven TENG). Comparison of experimental results from the CS mode TENG and transformed SE mode TENG. (g) Schematic diagram, (h) transferred charge and (i) current of the CS mode acoustic driven TENG. (j) Schematic diagram, (k) transferred charge and (l) current of the transformed SE mode acoustic driven TENG.

In the first case, the maximum energy output in a discharge process is:

$$
\begin{aligned}
E_{\mathrm{m}} = \int V \, \mathrm{d}q &= \frac{(\sigma_t + \sigma_t')d_0(z_2 - z_1)}{2\varepsilon_0(z_1\varepsilon_{\mathrm{r}} + d_0)} \cdot \frac{(\sigma_t + \sigma_t')\varepsilon_{\mathrm{r}} S d_0(z_2 - z_1)}{(z_1\varepsilon_{\mathrm{r}} + d_0)(z_2\varepsilon_{\mathrm{r}} + d_0)} \\
&= \frac{(\sigma_t + \sigma_t')^2 d_0^2(z_2 - z_1)^2 S}{2\varepsilon_0(z_1\varepsilon_{\mathrm{r}} + d_0)^2(z_2\varepsilon_{\mathrm{r}} + d_0)}
\end{aligned}
$$

(36)

According to the definition, the figure of merit for structures (FOM$_{\mathrm{S}}$) for the contact–separation mode TENG is:

$$
\mathrm{FOM_S} = \frac{2\varepsilon_0}{\sigma^2}\frac{E_{\mathrm{m}}}{Ax_{\mathrm{m}}} = \frac{d_0^2(z_2 - z_1)}{(z_1\varepsilon_{\mathrm{r}} + d_0)^2(z_2\varepsilon_{\mathrm{r}} + d_0)}
$$

(37)

Meanwhile, the figure of merit for materials (FOM$_{\mathrm{M}}$) and the figure of merit for performance (FOM$_{\mathrm{P}}$) are as follows:

$$
\mathrm{FOM_M} = \left(\sigma_t + \sigma_t'\right)^2
$$

(38)

$$\text{FOM}_{\text{P}} = \frac{2\varepsilon_0 d_0{}^2 (z_2 - z_1)}{(z_1 \varepsilon_{\text{r}} + d_0)^2 (z_2 \varepsilon_{\text{r}} + d_0)} \qquad (39)$$

It is worth noting that the FOM_{M} introduced in the literature is σ^2, which is derived from a TENG model similar to that in Fig. 3(d). We can get the same result if the model in Fig. 3(d) is used, while eqn (38) is more general. The dimensionless property of FOM_{S} can be validated using the basic parameters. The consistency means the proposed model and analytical approach can solve practical problems for TENGs, especially, with the rigorous mechanism, to analyze characteristics for TENGs when basic parameters are not finalized.

Comparison between infinite plate models and finite plate models

In the previous sections, infinite plate models have been utilized to analyze the TENG performance. In this section, infinite plate models will be compared with finite plate models to evaluate their accuracy and differences. For infinite plate models, the electric field is uniform, directed along the z-axis (see Note S18, ESI†). However, for finite plate models, neither the magnitude nor the direction of the electric field is uniform. It should be noted that the model used for Fig. 4 has infinite element domains to make sure that it is an infinite plate model, while a large air space is designed to make sure that the electric field distribution from the TENG is slightly influenced (can be neglected) by the space boundary. Other parameters for the TENG models in the two simulations are identical. The comparisons are conducted between the simulation results from Fig. 4 and 7. When the TENG size is obviously larger than its internal distance, the simulation model is shown in Fig. 7(a) (note that for the infinite plate model, large electric field intensities appear at the corners, causing different color bars). The electric field distribution is different from that of the infinite plate model (Fig. 4(d)), while the z-direction component of the electric field along the midline is similar (compare Fig. 7(b) with Fig. 4(e)), especially for the internal electric field E_2 and E_3.

The finite plate model is applied to estimate the performance of the TENG (corresponding to the infinite models introduced in Fig. 6, 4(f)–(h) and Note S10, ESI†). The two different models are compared in Note S19 (ESI†). Although the
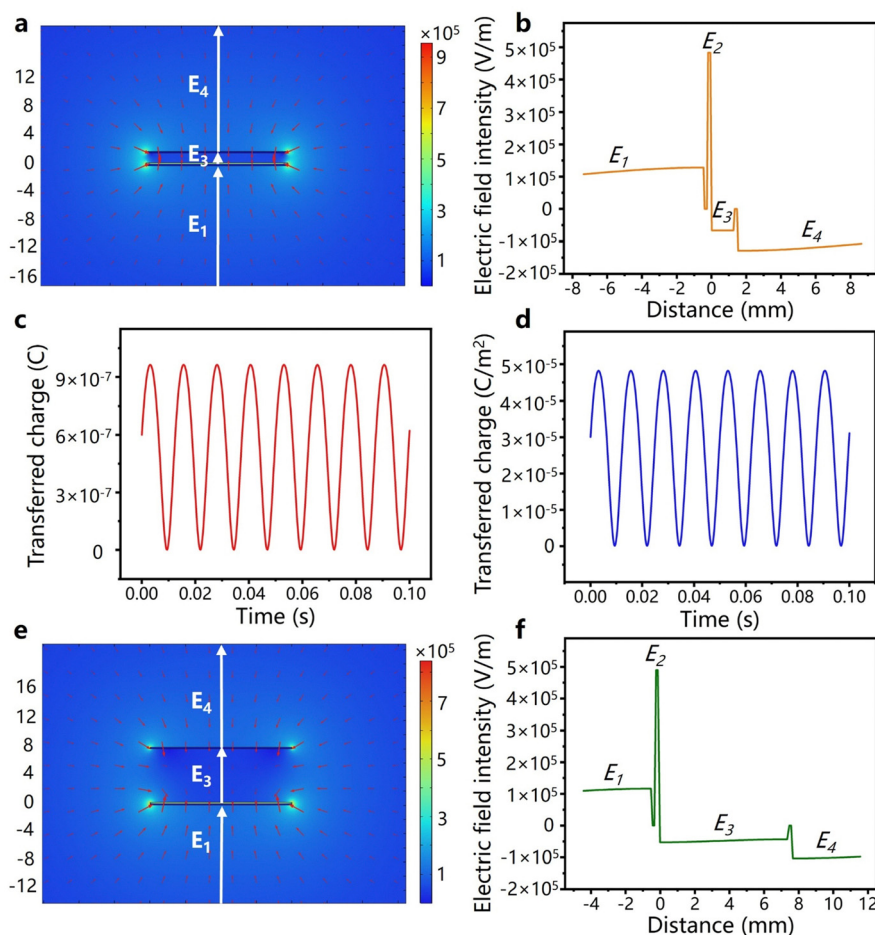

Fig. 7 Analysis of the finite plate model. (a) Simulation of the electric field distribution and (b) variation of the electric field intensity with distance for the finite plate model which has a small internal distance. (c) Transferred charge and (d) transferred charge per unit area (for the output electrode) calculated based on the simulation data. (e) Simulation of the electric field distribution and (f) variation of the electric field intensity with distance for the finite plate model which has a larger internal distance.
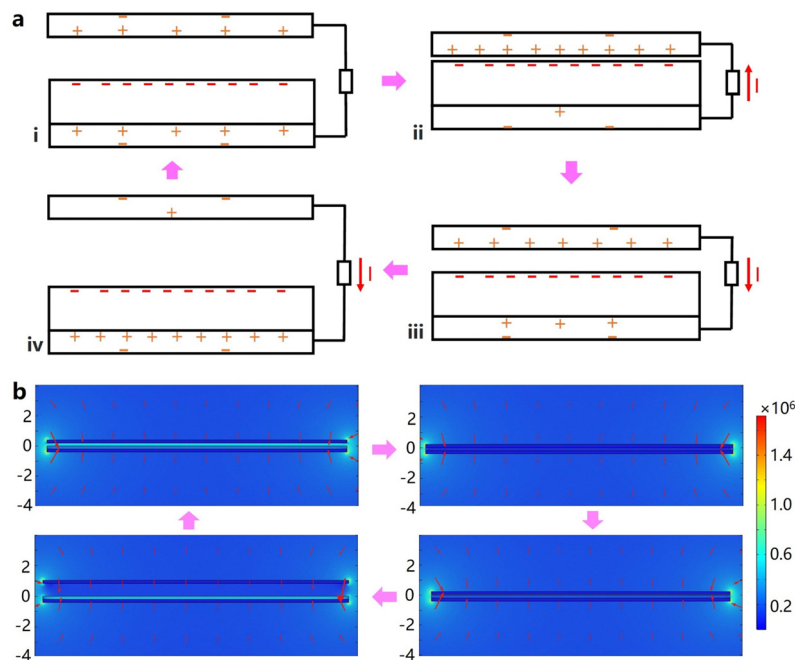
Fig. 8 Working principle and simulations for the TENG. (a) Schematic diagram of the working principle and (b) finite element simulation for the contact-separation mode TENG.

electric field distribution in the finite plate model shows significant difference to those in the infinite plate model, the mostly uniform electric field inside the TENG of the finite plate model is very similar to that of the infinite plate model (Note S19, ESI†). This should be attributed to its large size (20 mm) relative to the internal distance (0.1 mm). In this case, the transferred charge and transferred charge per unit area (transferred charge divided by the area of the electrode) of the TENG from simulation are shown in Fig. 7(c) and (d). The comparison of Fig. 7(d) and 4(h) shows that the transferred charge calculated from the finite plate model is very close to that from the infinite plate model. When the electrode distance is comparable to the TENG size, the simulated electric field is shown in Fig. 7(e) and (f). The electric field inside the TENG exhibits non-uniformity in both magnitude and direction. These are significantly different from those simulated with the infinite plate model (see Note S20, ESI†).

Therefore, utilizing the infinite plate model to evaluate the output performance of TENGs greatly reduces the analysis intensity with acceptable accuracy, especially in predicting the performance of TENG sensors with sizes much larger than electrode distances. While for a TENG with larger electrode distance, the finite plate model, along with electrodynamics approach (will be introduced in the next section) should be used. In addition, based on the theoretical model and its solution, it is suggested that the schematic diagram showing the working principle of the contact-separation mode TENG should be as depicted in Fig. 8(a). Compared with the common schematic diagrams (only one type of charge is distributed on each electrode, and the charge is drawn in the central region of

the electrode), the proposed schematic diagram better reflects actual charge distribution.

For many CS mode TENG sensors, if they are designed to detect small-scale variables (forces, motions, *etc.*), the internal distance of the TENG sensor will also be very small, like the acoustic sensor for robotics,[48] the paper based acoustic sensor,[49] the eye motion sensor,[50] the pulse sensor,[51] and the vibration sensor.[8] Even quite a few energy harvesters also have a small internal distance, like the wave energy harvester,[52] human motion harvester,[53] and TENG cardiac pacemaker.[54] The common point of these CS mode TENGs is that their sizes (centimeters) are much larger than their internal distances (hundreds of micrometers). The simulation for the CS mode TENG in a working cycle is shown in Fig. 8b. Due to the relatively small internal distances of the TENG compared to its size, variations in electric field are not significant. This is consistent with many TENG sensors in practice.

Electrodynamic model for the TENG

Solving the electrodynamic model is a more precise approach to predict the TENG performance, which works with any electrode size and electrode distance. This section adopts the same derivation method as in previous sections.

Charge redistribution takes place in all materials (see Note S21, ESI†). This process is instantaneous for conductors, while for dielectric materials, it may take considerable time, ranging from hours to even months. A previous study has revealed the bulk charge distribution inside dielectric materials of TENGs.[55] For the infinite plate model, it is not necessary to consider bulk charge distribution, as both surface and bulk charges have an equivalent effect on the electric field in space and on the charge
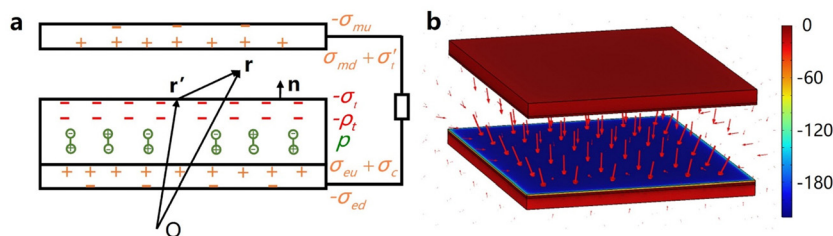
Fig. 9 Analysis of the electrodynamic model. (a) Schematic diagram of the TENG electrodynamic model. (b) The simulation result for the TENG based on the model.

transfer process. However, it makes a difference for the electrodynamic model. Considering the vast range of materials for TENGs, the distribution of bulk charge ρ_t and electric dipole p is implemented in the electrodynamic model.

The schematic diagram of the electrodynamic model is shown in Fig. 9(a). Based on the principle of electrostatic equilibrium, which requires zero electric field within the electrodes and equal potential between them, as well as charge conservation, the following equations can be written as:

$$-\sigma_{\mathrm{mu}} + \sigma_{\mathrm{md}} + \sigma_{\mathrm{eu}} - \sigma_{\mathrm{ed}} = -\sigma_t' + \sigma_c \tag{40}$$

where r denotes the position of the field point, while $\mathbf{r}'$ denotes the position of the source point. σ_{mu}, σ_{md}, σ_{eu}, and σ_{ed} represent the distribution of the charge density on two surfaces of the two electrodes, respectively. $\mathbf{r_{mo}}$ is the central position of the independent electrode. $\mathbf{r_{eo}}$ is that of the base electrode (for symmetric geometry. If not symmetric, $\mathbf{r_{mo}}$ and $\mathbf{r_{eo}}$ represent the internal points within the electrodes where electric fields generated by charges separated from that electrode cancelled out). S is the area and V is the volume for the materials, $\mathbf{n}$ is the unit vector perpendicular to the surface of the dielectric material, and $\mathbf{P}$ is the polarization electric field intensity generated

$$\begin{aligned}
&\frac{1}{4\pi\varepsilon_0}\int_S \frac{\sigma_{\mathrm{mu}}'(\mathbf{r_{mu}'})\cdot(\mathbf{r_{mo}}-\mathbf{r_{mu}'})}{|\mathbf{r_{mo}}-\mathbf{r_{mu}'}|^3}\mathrm{d}S' + \frac{1}{4\pi\varepsilon_0}\int_S \frac{\sigma_{\mathrm{mu}}'(\mathbf{r_{mu}'})\cdot(\mathbf{r_{mo}}-\mathbf{r_{mu}'})}{|\mathbf{r_{mo}}-\mathbf{r_{mu}'}|^3}\mathrm{d}S' + \frac{1}{4\pi\varepsilon_0}\int_S \frac{\sigma_t(\mathbf{r}_t')\cdot(\mathbf{r_{mo}}-\mathbf{r}_t')}{|\mathbf{r_{mo}}-\mathbf{r}_t'|^3}\mathrm{d}S' \\
&+ \frac{1}{4\pi\varepsilon_0}\int_V \frac{\rho_t(\mathbf{r}_t')\cdot(\mathbf{r_{mo}}-\mathbf{r}_t')}{|\mathbf{r_{mo}}-\mathbf{r}_t'|^3}\mathrm{d}V' + \frac{1}{4\pi\varepsilon_0}\oint_S \frac{\mathbf{P}(\mathbf{r_p'})\cdot\mathbf{n}\cdot(\mathbf{r_{mo}}-\mathbf{r_p'})}{|\mathbf{r_{mo}}-\mathbf{r_p'}|^3}\mathrm{d}S' + \frac{1}{4\pi\varepsilon_0}\int_V \frac{-\boldsymbol{\nabla}\cdot\mathbf{P}(\mathbf{r_p'})\cdot(\mathbf{r_{mo}}-\mathbf{r_p'})}{|\mathbf{r_{mo}}-\mathbf{r_p'}|^3}\mathrm{d}V' \\
&+ \frac{1}{4\pi\varepsilon_0}\int_S \frac{\sigma_{\mathrm{eu}}'(\mathbf{r_{eu}'})\cdot(\mathbf{r_{mo}}-\mathbf{r_{eu}'})}{|\mathbf{r_{mo}}-\mathbf{r_{eu}'}|^3}\mathrm{d}S' + \frac{1}{4\pi\varepsilon_0}\int_S \frac{\sigma_{\mathrm{ed}}'(\mathbf{r_{ed}'})\cdot(\mathbf{r_{mo}}-\mathbf{r_{ed}'})}{|\mathbf{r_{mo}}-\mathbf{r_{ed}'}|^3}\mathrm{d}S' = 0
\end{aligned} \tag{41}$$

$$\begin{aligned}
&\frac{1}{4\pi\varepsilon_0}\int_S \frac{\sigma_{\mathrm{mu}}'(\mathbf{r_{mu}'})\cdot(\mathbf{r_{eo}}-\mathbf{r_{mu}'})}{|\mathbf{r_{eo}}-\mathbf{r_{mu}'}|^3}\mathrm{d}S' + \frac{1}{4\pi\varepsilon_0}\int_S \frac{\sigma_{\mathrm{mu}}'(\mathbf{r_{md}'})\cdot(\mathbf{r_{eo}}-\mathbf{r_{md}'})}{|\mathbf{r_{eo}}-\mathbf{r_{md}'}|^3}\mathrm{d}S' + \frac{1}{4\pi\varepsilon_0}\int_S \frac{\sigma_t(\mathbf{r}_t')\cdot(\mathbf{r_{eo}}-\mathbf{r}_t')}{|\mathbf{r_{eo}}-\mathbf{r}_t'|^3}\mathrm{d}S' \\
&+ \frac{1}{4\pi\varepsilon_0}\int_V \frac{\rho_t(\mathbf{r}_t')\cdot(\mathbf{r_{eo}}-\mathbf{r}_t')}{|\mathbf{r_{eo}}-\mathbf{r}_t'|^3}\mathrm{d}V' + \frac{1}{4\pi\varepsilon_0}\oint_S \frac{\mathbf{P}(\mathbf{r_p'})\cdot\mathbf{n}\cdot(\mathbf{r_{eo}}-\mathbf{r_p'})}{|\mathbf{r_{eo}}-\mathbf{r_p'}|^3}\mathrm{d}S' + \frac{1}{4\pi\varepsilon_0}\int_V \frac{-\boldsymbol{\nabla}\cdot\mathbf{P}(\mathbf{r_p'})\cdot(\mathbf{r_{eo}}-\mathbf{r_p'})}{|\mathbf{r_{eo}}-\mathbf{r_p'}|^3}\mathrm{d}V' \\
&+ \frac{1}{4\pi\varepsilon_0}\int_S \frac{\sigma_{\mathrm{eu}}'(\mathbf{r_{eu}'})\cdot(\mathbf{r_{eo}}-\mathbf{r_{eu}'})}{|\mathbf{r_{eo}}-\mathbf{r_{eu}'}|^3}\mathrm{d}S' + \frac{1}{4\pi\varepsilon_0}\int_S \frac{\sigma_{\mathrm{ed}}'(\mathbf{r_{ed}'})\cdot(\mathbf{r_{eo}}-\mathbf{r_{ed}'})}{|\mathbf{r_{eo}}-\mathbf{r_{ed}'}|^3}\mathrm{d}S' = 0
\end{aligned} \tag{42}$$

$$\begin{aligned}
&\frac{1}{4\pi\varepsilon_0}\int_S \frac{\sigma_{\mathrm{mu}}'(\mathbf{r_{mu}'})}{|\mathbf{r_{mo}}-\mathbf{r_{mu}'}|}\mathrm{d}S' + \frac{1}{4\pi\varepsilon_0}\int_S \frac{\sigma_{\mathrm{mu}}'(\mathbf{r_{md}'})}{|\mathbf{r_{mo}}-\mathbf{r_{md}'}|}\mathrm{d}S' + \frac{1}{4\pi\varepsilon_0}\int_S \frac{\sigma_t(\mathbf{r}_t')}{|\mathbf{r_{mo}}-\mathbf{r}_t'|}\mathrm{d}S' + \frac{1}{4\pi\varepsilon_0}\int_V \frac{\rho_t(\mathbf{r}_t')}{|\mathbf{r_{mo}}-\mathbf{r}_t'|}\mathrm{d}V' \\
&+ \frac{1}{4\pi\varepsilon_0}\oint_S \frac{\mathbf{P}(\mathbf{r_p'})\cdot\mathbf{n}}{|\mathbf{r_{mo}}-\mathbf{r}_t'|}\mathrm{d}S' + \frac{1}{4\pi\varepsilon_0}\int_V \frac{-\boldsymbol{\nabla}\cdot\mathbf{P}(\mathbf{r_p'})}{|\mathbf{r_{mo}}-\mathbf{r}_t'|}\mathrm{d}V' + \frac{1}{4\pi\varepsilon_0}\int_S \frac{\sigma_{\mathrm{eu}}'(\mathbf{r_{eu}'})}{|\mathbf{r_{mo}}-\mathbf{r_{eu}'}|}\mathrm{d}S' + \frac{1}{4\pi\varepsilon_0}\int_S \frac{\sigma_{\mathrm{ed}}'(\mathbf{r_{ed}'})}{|\mathbf{r_{mo}}-\mathbf{r_{eu}'}|}\mathrm{d}S' \\
&= \frac{1}{4\pi\varepsilon_0}\int_S \frac{\sigma_{\mathrm{mu}}'(\mathbf{r_{mu}'})}{|\mathbf{r_{eo}}-\mathbf{r_{mu}'}|}\mathrm{d}S' + \frac{1}{4\pi\varepsilon_0}\int_S \frac{\sigma_{\mathrm{mu}}'(\mathbf{r_{md}'})}{|\mathbf{r_{eo}}-\mathbf{r_{md}'}|}\mathrm{d}S' + \frac{1}{4\pi\varepsilon_0}\int_S \frac{\sigma_t(\mathbf{r}_t')}{|\mathbf{r_{eo}}-\mathbf{r}_t'|}\mathrm{d}S' + \frac{1}{4\pi\varepsilon_0}\int_V \frac{\rho_t(\mathbf{r}_t')}{|\mathbf{r_{eo}}-\mathbf{r}_t'|}\mathrm{d}V' \\
&+ \frac{1}{4\pi\varepsilon_0}\oint_S \frac{\mathbf{P}(\mathbf{r_p'})\cdot\mathbf{n}}{|\mathbf{r_{eo}}-\mathbf{r_p'}|}\mathrm{d}S' + \frac{1}{4\pi\varepsilon_0}\int_V \frac{-\boldsymbol{\nabla}\cdot\mathbf{P}(\mathbf{r_p'})}{|\mathbf{r_{eo}}-\mathbf{r_p'}|}\mathrm{d}V' + \frac{1}{4\pi\varepsilon_0}\int_S \frac{\sigma_{\mathrm{eu}}'(\mathbf{r_{eu}'})}{|\mathbf{r_{eo}}-\mathbf{r_{eu}'}|}\mathrm{d}S' + \frac{1}{4\pi\varepsilon_0}\int_S \frac{\sigma_{\mathrm{ed}}'(\mathbf{r_{ed}'})}{|\mathbf{r_{eo}}-\mathbf{r_{ed}'}|}\mathrm{d}S'
\end{aligned} \tag{43}$$

Paper

by electric dipoles, which has important applications like ferroelectric material based TENGs[56] (more discussion is provided in Note S22, ESI†). Based on these equations, the charge distribution on the two electrodes can be analyzed.

The potential $\varphi(\mathbf{r})$ at any point can be evaluated by summing the potentials generated by the charges distributed in the dielectric material $\varphi_{\mathrm{m}}(\mathbf{r})$, independent electrode $\varphi_{\mathrm{d}}(\mathbf{r})$, and base electrode $\varphi_{\mathrm{e}}(\mathbf{r})$(detailed in Note S23, ESI†). Then the electric field intensity can be derived from the potentials:

$$\begin{aligned}\mathbf{E}(\mathbf{r}) &= -\boldsymbol{\nabla}\varphi(\mathbf{r}) \\ &= -\frac{\partial\varphi(\mathbf{r})}{\partial\mathbf{r}}\frac{\partial\mathbf{r}}{\partial x}\mathbf{e_x} - \frac{\partial\varphi(\mathbf{r})}{\partial\mathbf{r}}\frac{\partial\mathbf{r}}{\partial y}\mathbf{e_y} - \frac{\partial\varphi(\mathbf{r})}{\partial\mathbf{r}}\frac{\partial\mathbf{r}}{\partial z}\mathbf{e_z}\end{aligned} \qquad (44)$$

The transferred charge and the current between the two electrodes are:

$$Q = \int_{r_1}^{r_2}\mathrm{d}Q = \int_{r_1}^{r_2}\frac{\mathrm{d}[\sigma_{\mathrm{eu}} - \sigma_{\mathrm{ed}} - (\sigma_{\mathrm{md}} - \sigma_{\mathrm{mu}})]S}{2\mathrm{d}r}\mathrm{d}r \qquad (45)$$

$$I(t) = \frac{\mathrm{d}Q}{\mathrm{d}t} = \frac{\mathrm{d}Q}{\mathrm{d}r}v = \frac{\mathrm{d}[\sigma_{\mathrm{eu}} - \sigma_{\mathrm{ed}} - (\sigma_{\mathrm{md}} - \sigma_{\mathrm{mu}})]S}{2\mathrm{d}r}v \qquad (46)$$

The electrodynamic model is simulated as shown in Fig. 9(b). In the simulation, the dielectric material, electrodes and substrates are all finite plates. Different colors in the simulation diagram represent the distribution of the potential. The arrows are used to describe the distribution of electric field intensity. For the infinite plate models, the electric fields are uniform, and the direction of the electric field intensity is the same in one region, so we use the unit vector $\mathbf{e_z}$ to describe it. The analysis for the dynamic model is more complex, in which we use the special vector $\mathbf{r}$ ($\mathbf{r} = r_x\mathbf{e_x} + r_y\mathbf{e_y} + r_z\mathbf{e_z}$, where r_x, r_y, and r_z are the components of $\mathbf{r}$ in x, y, and z axis respectively) to describe the magnitude and direction. So, the electric field intensities for the electrodynamic model have three independent directions. In the simulation diagram, the direction of the arrow represents the direction of the electric field intensity at the point of the arrow root, and the density of the arrows means the magnitude of the electric field intensity. In the middle line of the model, the direction of the electric field intensity is nearly along the line (pointing at $\mathbf{e_z}$ direction), while at the edge of the model, the arrows point at different positions. Comparing the electrodynamic model with the infinite plate models, the electrodynamic model is a more precise approach to predict the TENG performance, which works with any electrode size and electrode distance. The solution of charge and electric field distributions is based on the electrodynamic methods, which is computationally intensive. The infinite plate model approach significantly simplifies calculations while maintaining sufficient accuracy when the size of the TENG is much larger than its internal distance. Intuitive analytical solutions can be obtained from infinite plate models, while finite plate models usually only have numerical solutions (like the result in Fig. 9b).

Practical applications based on the proposed theory

In this section, three applications based on the theory are analyzed. They are the effect of the pre-charging charges, variation of the output performance with the working frequency, and the explanation for the TENG-based electric field communication. These show the good practicability of the theory, and also further verify the validity of the theory.

(1) The effect of the pre-charging charges. In the section of "Comparative analysis for two types of CS mode TENGs", it has been proved that pre-charging charges play important roles in TENGs in theory. The schematic diagrams are shown in Fig. 10a–b. The TENG with a pre-charging dielectric material has larger charge distribution in each surface and will have more transferred charges when the two materials are in contact-separation motion. Since the dielectric materials used to fabricate TENGs usually have strong electronegativity, they easily gain electrons from other materials in the environment (like paper and human hand). Pre-charging charges can be acquired for the dielectric material by the triboelectrification process. The comparison between the original FEP film and the pre-charging FEP film (with the PET material) is shown in Note S24 (ESI†). The pre-charging FEP film has a high surface potential, indicating that there have been more surface charges on the material. The two types of FEP films are used to fabricate acoustic driven TENGs, and the output performance of the TENGs are compared in Fig. 10e and f. Obviously, the voltage and transferred charge of the TENG with a pre-charging dielectric material are much larger than those of the TENG with a normal dielectric material. Therefore, the theory and experiments all show that pre-charging charges on the dielectric material can improve the output performance of the TENG, providing an approach to fabricate high-performance TENGs in practice.

(2) Variation of the output performance with the working frequency. If the movement of the TENG is regarded as a sinusoidal motion: $z(t) = A\sin(\omega t + \varphi)$, then

$$I(t) = \frac{(\sigma_t + \sigma_t')\varepsilon_{\mathrm{r}}Sd_0}{(z\varepsilon_{\mathrm{r}} + d_0)^2}2\pi Af\cos(2\pi ft + \varphi) \qquad (47)$$

We can see that the current is proportional to the working frequency of the TENG, while the voltage is related to the position z but not the frequency (in the situation where frequencies influence the movement of the TENG, like in resonance, the voltage is also affected by the position intrinsically). Irregular motions can be expressed according to the Fourier series:

$$z(t) = \sum_{k=1}^{n} a_k\sin(k\omega t + \varphi_k) \qquad (48)$$

Then the current can be derived as:

$$I(t) = 2\pi f\sum_{k=1}^{n} ka_k\cos(2\pi kt + \varphi_k) \qquad (49)$$

It is still proportional to the frequency. A previous study[57] has shown the relationship of the output performance of the CS
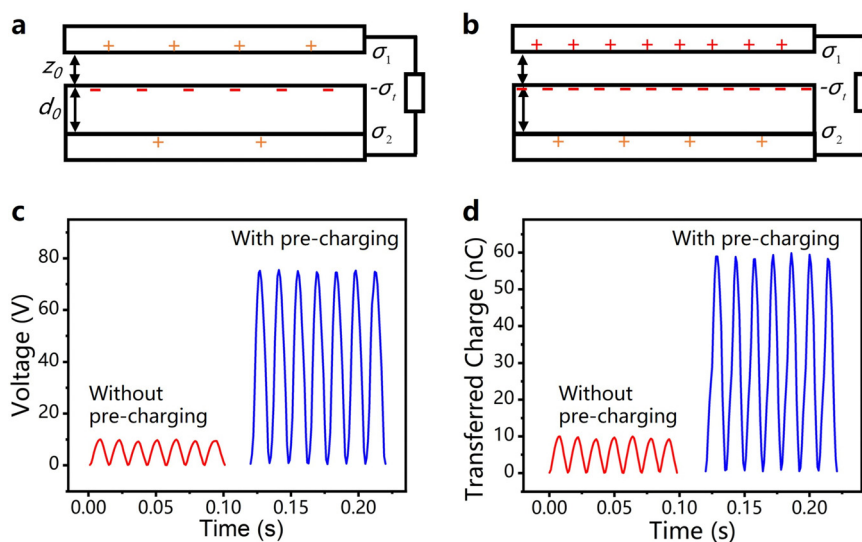
Fig. 10 The effect of the pre-charging charges. (a) Schematic diagram of the TENG with the pre-charging dielectric material. (b) Schematic diagram of the TENG with more pre-charging charges on the dielectric material. Comparison of the (c) voltage, (d) transferred charge of the TENG with normal FEP material and pre-charging FEP material.
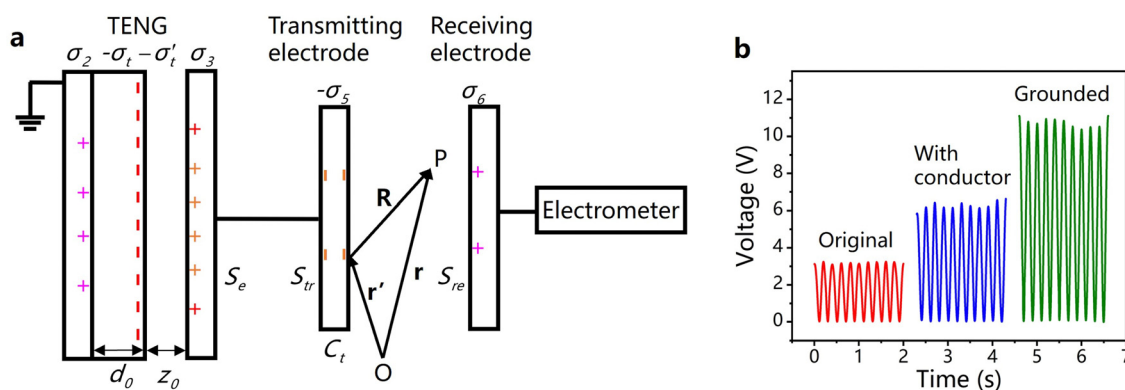

Fig. 11 Analysis of the TENG-based communication. (a) Theoretical model for the TENG-based communication system. (b) The electrical signals received by the receiving electrode.

mode TENG with the frequency. As the frequency increases, the current is approximately proportional to the frequency while the voltage remains the same. Therefore, the theory can explain the output performance of the TENG with the frequency.

(3) Explanation for the TENG-based electric field communication. TENG-based electric field communication has attracted many researchers in the TENG field due to its interestingness.[58,59] But corresponding theories are still inadequate, and many phenomena cannot be explained. A recent study[60] has introduced an approach for TENG-based electric field communication. The TENG is in contact-separation motion by a linear motor. One electrode of the TENG is grounded and another electrode is connected to the transmitting electrode. The electric field in the space can be received by the receiving electrode, which is connected to the electrometer (details are shown in Note S25, ESI†). But we do not know why

one electrode of the TENG should be grounded, so this will be explained based on the proposed theory.

The theoretical model of the TENG-based communication system is shown in Fig. 11. When the base electrode on the dielectric material is not grounded, the model for the TENG is shown in Note S25 (ESI†). Based on the analysis of Fig. 4aii in the manuscript and Note S8 (ESI†), we can get the charge density on the transmitting electrode:

$$\sigma_5 = \frac{(\sigma_t - \sigma_c)S_e}{2S_t} \quad (50)$$

It is not related to the internal distance of the TENG, so in this model, the radiated electric field remains unchanged when the TENG moves. While when one electrode is grounded, as shown in Fig. 11a, to fulfill the electrostatic equilibrium of the independent electrode of the TENG and the transmitting

electrode, we can get

$$
\begin{cases}
\dfrac{\sigma_2}{2\varepsilon_0} - \dfrac{\sigma_t + \sigma_t'}{2\varepsilon_0} + \dfrac{\sigma_3}{2\varepsilon_0} = 0 \\[2mm]
-\left(\dfrac{\sigma_2}{2\varepsilon_0} + \dfrac{\sigma_t + \sigma_t'}{2\varepsilon_0} - \dfrac{\sigma_3}{2\varepsilon_0}\right)d_0 - \left(\dfrac{\sigma_2}{2\varepsilon_0} - \dfrac{\sigma_t + \sigma_t'}{2\varepsilon_0} - \dfrac{\sigma_3}{2\varepsilon_0}\right)z_0 = \dfrac{(\sigma_3 - \sigma_t')S_e}{C_t}
\end{cases}
\tag{51}
$$

where C_t is the capacitance of the transmitting electrode, and S_e is the area of the independent electrode. The solution is

$$
\begin{cases}
\sigma_2 = \dfrac{(\sigma_t + \sigma_t')z_0 C_t - \sigma_t \varepsilon_0 S_e}{d_0 C_t + z_0 C_t - \varepsilon_0 S_e} \\[3mm]
\sigma_3 = \dfrac{(\sigma_t + \sigma_t')d_0 C_t - \sigma_t' \varepsilon_0 S_e}{d_0 C_t + z_0 C_t - \varepsilon_0 S_e}
\end{cases}
\tag{52}
$$

The charge density on the transmitting electrode is

$$
\sigma_5 = \frac{(\sigma_t + \sigma_t')d_0 C_t S_e - \sigma_{te}\varepsilon_0 S_e^2}{2S_t(d_0 C_t + z_0 C_t - \varepsilon_0 S_e)}
\tag{53}
$$

In this case, the charge density on the transmitting electrode changes with the internal distance of the TENG, and thus an alternative electrical signal can be received by the receiving electrode. If the base electrode on the dielectric material is not grounded but connected to a conductor with a capacitance of C_s, we can derive the charge density on the transmitting electrode as follows:

$$
\sigma_5 = \frac{\left(-(\sigma_t + \sigma_t')\varepsilon_0 C_t S_b + \sigma_c \varepsilon_0 C_t S_b + \sigma_t d_0 C_s C_t - \sigma_t' \varepsilon_0 C_s S_e\right)S_e}{2S_t(-\varepsilon_0 C_t S_b + d_0 C_s C_t - \varepsilon_0 C_s S_e + z_0 C_s C_t)}
\tag{54}
$$

In this case, the charge density on the transmitting electrode changes with the internal distance of the TENG, but the value is less than that from eqn (53). The electric field can be radiated when the charges are on the transmitting electrode:

$$
E_p = \frac{1}{4\pi\varepsilon_0} \oint_{S_{tr}} \frac{-\sigma_5(r') \cdot (r - r')}{|r - r'|^3} dS'
\tag{55}
$$

The equation shows that the radiated electric field decays quadratically with the distance, while the received electrical signals may decay logarithmically.

The equations are derived based on the infinite plate models. For the TENG-based communication experiment, when the TENG is in contact-separation motion, it can be regarded as a combination of the infinite plate model (when the size is much larger than the internal distance) and finite plate model. Therefore, when the base electrode is not grounded, the electrical signal received by the receiving electrode will be very small. When the base electrode is grounded, the received signal will be much larger. When the base electrode is connected to a conductor, the received signal will be larger than the first case while smaller than the second case.

Experiments are designed to verify this. The details of the experiment are provided in Note S25 (ESI†). The experimental results are shown in Fig. 11b. When the base electrode is not connected to

other things, the electrical signal received by the receiving electrode is small, while when the based electrode is grounded, the received signal becomes much larger. Therefore, the experimental results are consistent with the theoretical analysis. This study provides a demonstration to use the theories in practical scenario.

Conclusion

In summary, this study has presented a systematic theoretical analysis with solid mathematical derivations for contact-separation mode TENGs. It is the authors' insight that the multiple variables to describe the charge densities on the TENG usually include initial charges and induced charges. The multiple variables can be unified into less variables based on initial source charges that determine the electric field of the CS mode TENG necessarily and sufficiently. Using the essential variables, the study has created models for the electric field of the CS mode TENG (validated convincingly in the rest of the paper), which precisely addresses the charge transfer of the CS mode TENG in motion or under deformation.

Starting from the infinite plate model, the charge distribution of both the dielectric material and the independent electrode resulting from CE is determined first. On top of it, three types of models are proposed so that various forms of contact-separation mode TENGs can be covered. Charge distribution/redistribution (not random but restrained by initial source charges) and the charge transfer process are explained by the mechanism. Both the conduction current in the external circuit and the displacement current inside the TENG can be deduced rigorously. And equations are deduced step by step rigorously according to basic physical theorems. The study introduced the ''predicted characteristics correlating'' method to validate the theoretical models and the analytical solutions. The theoretically predicted TENG characteristics are all consistent with the actual phenomena in practice. This indicates that the highly accurate theoretical analysis could also be the framework for better understanding of the practical performances of TENGs. The applicability of various models is discussed by comparing the simulation and analytical results from infinite plate models and those from finite plate models. On top of it, a set of more accurate schematic diagrams for the working principle of TENGs is first proposed. Then, an electrodynamic model with its solving approach is proposed, which is applicable for contact-separation mode TENGs of any size. Finally, applications are analyzed based on the proposed theory, showing the theory may provide guidance for TENGs in practice.

Basic theories have always set important foundations. This study has analyzed that infinite plate models and their equations can be used for designing TENGs in practice. This simplifies calculations while maintaining sufficient accuracy. But it should be noted that infinite plate models are solved based on an assumption that the charge/electric field distribution is uniform. They are analyzed in an ideal situation and cannot match the actual experiment 100%. The study also analyzed some classical cases with the proposed approaches

as necessary steps to make the theoretical framework complete and rigorous. The analysis from the theory shows that to increase the output of the TENG, the initial charging from contact electrification and pre-charging of the dielectric material should be increased while considering suitable internal distance. The expected characteristics of the TENG, and the charge distribution and charge transfer process of the TENG can be analyzed using the theoretical approaches proposed in this study. Therefore, the study could be a part of a rigorous, applicable and extensible theoretical foundation for TENGs.

Experimental section

Fabrication of the acoustic driven TENG and measurement equipment

The acoustic driven TENG consists of a modified Helmholtz resonant cavity, an aluminum film with acoustic holes, and a FEP film with a conductive ink-printed electrode. The conductive ink is composed of carbon and other conductive particles. The conductive ink-printed electrode is about 5 micrometers, with good conductivity. The FEP film with the electrode is relatively low-cost, easy-fabricated, flexible, and easy to vibrate with the acoustic wave. The resonant cavity has dimensions of 73 mm × 73 mm × 40 mm. Two tubes with an inner diameter of 5.0 mm and a length of 32 mm are fixed on the resonant cavity. The aluminum film with uniformly distributed acoustic holes is used as the electropositive triboelectric layer. The length, width, and thickness of the film are 45 mm, 45 mm, and 0.1 mm, respectively. The FEP film is used as the electronegative triboelectric layer due to its strong electronegativity and good flexibility. A screen-printing device is used to print the conductive ink (CH-8(MOD2)) on the FEP film (WitLan). The shell is printed using a 3D printer with the PLA material.

When measuring the electrical output of the TENG, the device was mounted on an optical plate with a loudspeaker, which is driven by a sinusoidal wave from a function generator (YE1311). The output signals, including the open-circuit voltage, short-circuit current, and transferred charges, are measured using a Keithley 6514 electrometer.

Simulation approaches

COMSOL Multiphysics software is used for all the finite element simulations in this study. As we have derived the theoretical equations, we can obtain the analytical results directly. To achieve the numerical result (as verification), the boundary conditions are set up based on the problem in the software, while the governing equations are not changed. In this way, the simulation results are independent solutions to the same problem and therefore can be used as the verification and visualization for the analytical results.

The AD/DC modules, electrostatic interfaces and steady state analysis are adopted in these simulations. For the infinite plate models, in addition to setting the normal simulation area, all edges of the simulation model should be set as infinite element domains. Fig. 12a shows the details in simulating Fig. 3b. The dielectric layer is set as the FEP material, and the conductive electrodes are set on the lower side and upper side of the dielectric material, respectively. With the infinite element domains, the dielectric layer and the electrode are infinite large plates for numerical simulations. Other spaces are filled with air and also infinite large in numerical simulations. Fig. 3c is from the same simulation model but with different charge distribution on the dielectric layer and the electrode.

Fig. 12b shows the details of the simulation image corresponding to Fig. 3e in the manuscript. Fig. 12a shows the simulation result for tribo-charge layers, while Fig. 12b shows
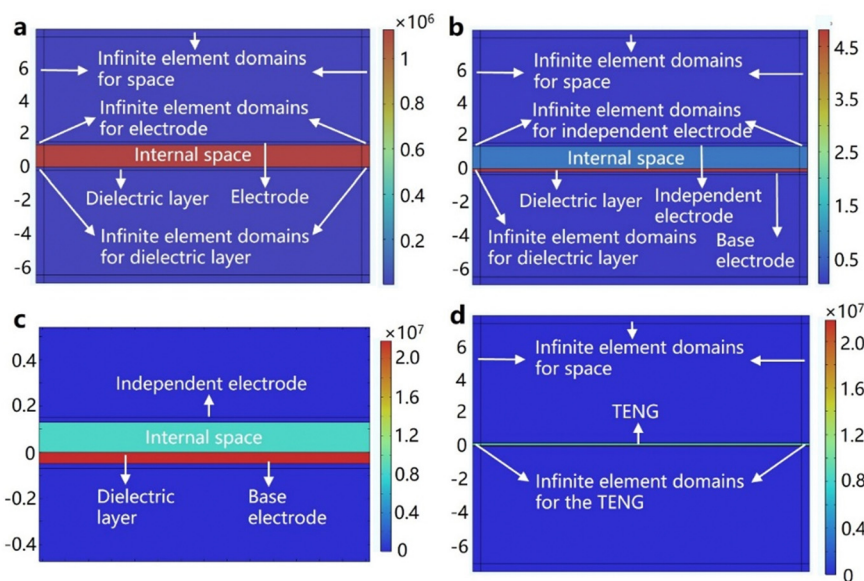

Fig. 12 Detailed explanation for simulation images from infinite plate models. Detailed explanation for the model structure corresponding to (a) the simulation image Fig. 3b, (b) the simulation image Fig. 3e, and (c) and (d) the simulation image Fig. 6b.
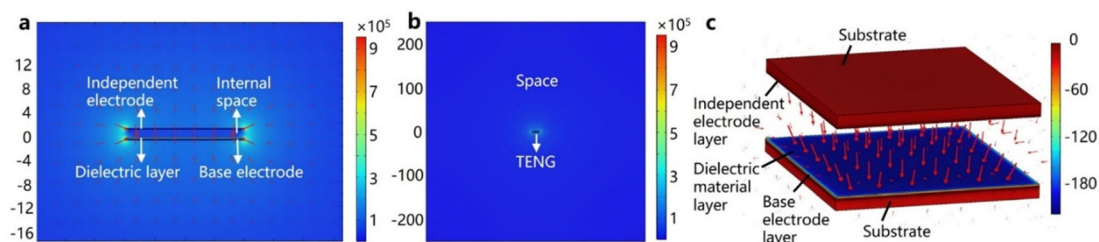
Fig. 13 Model structure designed in simulations corresponding to (a) and (b) the simulation image Fig. 7a, and (c) the simulation image Fig. 9b.

the simulation result for a TENG. The infinite large plates for the simulation model in Fig. 12b are the independent electrode, dielectric layer and base electrode. Different colors represent different electric field intensities. Uniform electric field is formed in each space because infinite plate models are used in numerical simulations. Comparing Fig. 3e with Fig. 3f, at the upper surface of the dielectric material distance = 0. $\mathbf{E_1}$ and $\mathbf{E_4}$ represent electric fields in outer spaces, $\mathbf{E_2}$ represents the electric field inside the dielectric material, and $\mathbf{E_3}$ is the electric field at the internal space of the TENG. They are vectors with magnitudes and directions, while E_1, E_2, E_3 and E_4 are scalar electric field intensities. Fig. 3h, 4b and d can be analyzed in the same way.

Corresponding to the simulation image Fig. 7a, the model structure designed in the simulation is shown in Fig. 13a and b. The top layer is the independent electrode and bottom layers are the dielectric material and base electrode. Fig. 13a is a part of the whole model shown in Fig. 13b. Unlike infinite plate models, infinite element domains are not used for finite plate models, but a large air space is set to make sure that the electric field distribution from the TENG is slightly influenced (can be neglected) by the space boundary. It should be noted that for the simulation image from the finite plate model, large electric field intensities appear at the corners due to the edge effect, corresponding to very different color bars compared with that from the infinite plate model.

For the three-dimensional simulation corresponding to the simulation image Fig. 9b, the structure simulated is shown in Fig. 13c. To design thin layers (50 μm for dielectric layer and electrodes) for the three-dimensional model, two cuboids with dimensions 6 mm × 6 mm × 0.4 mm are utilized as substrates, and thin layers can be designed using the "layer" function in COMSOL software. Both surface charge distribution and bulk charge distribution are setup for the dielectric material layer, and the complex electric field distribution inside the TENG from the independent electrode to the dielectric material can be shown from the simulation.

For all calculations and simulations in the study, the dielectric permittivity is set as 2.2. If we want to analyze TENGs with other dielectric materials, we can input the practical values to parameters including dielectric permittivity, thickness, and charge density (according to the actual situation). We focus on the charge distribution of the TENG in a steady state. Since that the charge transfer velocity is much faster than the movement velocity of the TENG, the charge transfer process of the

TENG can be seen as a quasistatic process. Therefore, for the conductive electrode (Al, Cu, Au, conductive ink, or other material with good conductivity) in electrostatic analysis, we always think that they are in electrostatic equilibrium states with zero electric field intensity (and equal potential if the two electrodes are connected). Once the model for the dielectric material and conductive electrodes have been developed, we can substitute specific values into parameters according to the actual situation of the TENG device, so the influence of different materials can be accounted.

Author contributions

Data availability

All data needed to evaluate the conclusions in the paper are present in the paper and/or the ESI.† Additional data related to this paper may be requested from the authors.

Conflicts of interest

The authors declare that they have no competing interests.

Acknowledgements

References

1 W. Xu, H. Zheng, Y. Liu, X. Zhou, C. Zhang, Y. Song, X. Deng, M. Leung, Z. Yang, R. X. Xu, Z. L. Wang, X. C. Zeng and Z. Wang, *Nature*, 2020, **578**, 392–396.

2 Z. L. Wang, *Nature*, 2017, **542**, 159–160.

3 R. Hinchet, H.-J. Yoon, H. Ryu, M.-K. Kim, E.-K. Choi, D.-S. Kim and S.-W. Kim, *Science*, 2019, **365**, 491–494.

4 Z. Wen, M.-H. Yeh, H. Guo, J. Wang, Y. Zi, W. Xu, J. Deng, L. Zhu, X. Wang, C. Hu, L. Zhu, X. Sun and Z. L. Wang, *Sci. Adv.*, 2016, **2**, e1600097.

5 I.-Y. Suh, Y.-J. Kim, P. Zhao, D. S. Cho, M. Kang, Z.-Y. Huo and S.-W. Kim, *Nano Energy*, 2023, **110**, 108343.

6 H. Qiu, H. Wang, L. Xu, M. Zheng and Z. L. Wang, *Energy Environ. Sci.*, 2023, **16**, 473–483.

7 C. Rodrigues, D. Nunes, D. Clemente, N. Mathias, J. M. Correia, P. Rosa-Santos, F. Taveira-Pinto, T. Morais, A. Pereira and J. Ventura, *Energy Environ. Sci.*, 2020, **13**, 2657–2683.

8 H. Zhao, M. Shu, Z. Ai, Z. Lou, K. W. Sou, C. Lu, Y. Jin, Z. Wang, J. Wang, C. Wu, Y. Cao, X. Xu and W. Ding, *Adv. Energy Mater.*, 2022, **12**, 2270154.

9 Y. J. Kim, J. Lee, J. H. Hwang, Y. Chung, B. J. Park, J. Kim, S. H. Kim, J. Mun, H. J. Yoon, S. M. Park and S. W. Kim, *Adv. Mater.*, 2024, **36**, e2307194.

10 L. Yin, K. N. Kim, J. Lv, F. Tehrani, M. Lin, Z. Lin, J. M. Moon, J. Ma, J. Yu, S. Xu and J. Wang, *Nat. Commun.*, 2021, **12**, 1542.

11 J. Luo, W. Gao and Z. L. Wang, *Adv. Mater.*, 2021, **33**, e2004178.

12 S. A. Hashemi, S. Ramakrishna and A. G. Aberle, *Energy Environ. Sci.*, 2020, **13**, 685–743.

13 H. Ryu, H. M. Park, M. K. Kim, B. Kim, H. S. Myoung, T. Y. Kim, H. J. Yoon, S. S. Kwak, J. Kim, T. H. Hwang, E. K. Choi and S. W. Kim, *Nat. Commun.*, 2021, **12**, 4374.

14 J. Zhu, S. Ji, J. Yu, H. Shao, H. Wen, H. Zhang, Z. Xia, Z. Zhang and C. Lee, *Nano Energy*, 2022, **103**, 107766.

15 T. Jin, Z. Sun, L. Li, Q. Zhang, M. Zhu, Z. Zhang, G. Yuan, T. Chen, Y. Tian, X. Hou and C. Lee, *Nat. Commun.*, 2020, **11**, 5381.

16 D. Doganay, M. O. Cicek, M. B. Durukan, B. Altuntas, E. Agbahca, S. Coskun and H. E. Unalan, *Nano Energy*, 2021, **89**, 106412.

17 P. Pandey, K. Thapa, G. P. Ojha, M.-K. Seo, K. H. Shin, S.-W. Kim and J. I. Sohn, *Chem. Eng. J.*, 2023, **452**, 139209.

18 C. Chen, Z. Wen, J. Shi, X. Jian, P. Li, J. T. W. Yeow and X. Sun, *Nat. Commun.*, 2020, **11**, 4143.

19 H. Zhao, M. Xu, M. Shu, J. An, W. Ding, X. Liu, S. Wang, C. Zhao, H. Yu, H. Wang, C. Wang, X. Fu, X. Pan, G. Xie and Z. L. Wang, *Nat. Commun.*, 2022, **13**, 3325.

20 Z. L. Wang, *Adv. Energy Mater.*, 2020, **10**, 2000137.

21 Z. L. Wang, *Mater. Today*, 2017, **20**, 74–82.

22 J. Shao, M. Willatzen and Z. L. Wang, *J. Appl. Phys.*, 2020, **128**, 111101.

23 J. Peng, S. D. Kang and G. J. Snyder, *Sci. Adv.*, 2017, **3**, eaap8576.

24 C. Xu, Y. Zi, A. C. Wang, H. Zou, Y. Dai, X. He, P. Wang, Y. C. Wang, P. Feng, D. Li and Z. L. Wang, *Adv. Mater.*, 2018, **30**, e1706790.

25 H. Zhang, L. Quan, J. Chen, C. Xu, C. Zhang, S. Dong, C. Lü and J. Luo, *Nano Energy*, 2019, **56**, 700–707.

26 W. Sun, Z. Jiang, X. Xu, Q. Han and F. Chu, *Int. J. Non Linear Mech.*, 2021, **136**, 103773.

27 Y. Zi, C. Wu, W. Ding and Z. L. Wang, *Adv. Funct. Mater.*, 2017, **27**, 1700049.

28 A. Ghaffarinejad and J. Yavand Hasani, *Appl. Phys. A*, 2019, **125**, 1–14.

29 B. Yang, W. Zeng, Z. H. Peng, S. R. Liu, K. Chen and X. M. Tao, *Adv. Energy Mater.*, 2016, **6**, 1600505.

30 A. Ghaffarinejad, J. Y. Hasani, R. Hinchet, Y. Lu, H. Zhang, A. Karami, D. Galayko, S.-W. Kim and P. Basset, *Nano Energy*, 2018, **51**, 173–184.

31 R. Hinchet, A. Ghaffarinejad, Y. Lu, J. Y. Hasani, S.-W. Kim and P. Basset, *Nano Energy*, 2018, **47**, 401–409.

32 S. Niu, S. Wang, L. Lin, Y. Liu, Y. S. Zhou, Y. Hu and Z. L. Wang, *Energy Environ. Sci.*, 2013, **6**, 3576.

33 J. Shao, M. Willatzen, Y. Shi and Z. L. Wang, *Nano Energy*, 2019, **60**, 630–640.

34 R. D. I. G. Dharmasena, K. D. G. I. Jayawardena, C. A. Mills, J. H. B. Deane, J. V. Anguita, R. A. Dorey and S. R. P. Silva, *Energy Environ. Sci.*, 2017, **10**, 1801–1811.

35 X. Chen, F. Zhang, C. Han, Y. Liu, G. Y. Chen, X. Sun and Z. Wen, *Nano Energy*, 2023, **111**, 108435.

36 Y. Zi, S. Niu, J. Wang, Z. Wen, W. Tang and Z. L. Wang, *Nat. Commun.*, 2015, **6**, 8376.

37 J. Shao, Y. Yang, O. Yang, J. Wang, M. Willatzen and Z. L. Wang, *Adv. Energy Mater.*, 2021, **11**, 2100065.

38 Z. Liu, Y. Huang, Y. Shi, X. Tao, H. He, F. Chen, Z. X. Huang, Z. L. Wang, X. Chen and J. P. Qu, *Nat. Commun.*, 2022, **13**, 4083.

39 J. Kim, D. Kang, H. K. Lee, J. H. Hwang, H. Y. Lee, S. Jeon, D. Kim, S. Kim and S. W. Kim, *Adv. Funct. Mater.*, 2022, **33**, 2209648.

40 D. Kang, H. Y. Lee, J.-H. Hwang, S. Jeon, D. Kim, S. Kim and S.-W. Kim, *Nano Energy*, 2022, **100**, 107531.

41 Z. L. Wang and A. C. Wang, *Mater. Today*, 2019, **30**, 34–51.

42 H. Wang, Z. Fan, T. Zhao, J. Dong, S. Wang, Y. Wang, X. Xiao, C. Liu, X. Pan, Y. Zhao and M. Xu, *Nano Energy*, 2021, **84**, 105920.

43 X. Xiao, X. Zhang, S. Wang, H. Ouyang, P. Chen, L. Song, H. Yuan, Y. Ji, P. Wang, Z. Li, M. Xu and Z. L. Wang, *Adv. Energy Mater.*, 2019, **9**, 1902460.

44 Z. Wen, J. Chen, M.-H. Yeh, H. Guo, Z. Li, X. Fan, T. Zhang, L. Zhu and Z. L. Wang, *Nano Energy*, 2015, **16**, 38–46.

45 M. Xu, T. Zhao, C. Wang, S. L. Zhang, Z. Li, X. Pan and Z. L. Wang, *ACS Nano*, 2019, **13**, 1932–1939.

46 H. Zhao, X. Xiao, P. Xu, T. Zhao, L. Song, X. Pan, J. Mi, M. Xu and Z. L. Wang, *Adv. Energy Mater.*, 2019, **9**, 1902824.

47 W. He, X. Fu, D. Zhang, Q. Zhang, K. Zhuo, Z. Yuan and R. Ma, *Nano Energy*, 2021, **84**, 105880.

48 H. Guo, X. Pu, J. Chen, Y. Meng, M.-H. Yeh, G. Liu, Q. Tang, B. Chen, D. Liu, S. Qi, C. Wu, C. Hu, J. Wang and Z. L. Wang, *Sci. Rob.*, 2018, **3**, eaat2516.

49 X. Fan, J. Chen, J. Yang, P. Bai, Z. Li and Z. L. Wang, *ACS Nano*, 2015, **9**, 4236–4243.

50 X. Pu, H. Guo, J. Chen, X. Wang, Y. Xi, C. Hu and Z. L. Wang, *Sci. Adv.*, 2017, **3**, e1700694.

51 J. Yang, J. Chen, Y. Su, Q. Jing, Z. Li, F. Yi, X. Wen, Z. Wang and Z. L. Wang, *Adv. Mater.*, 2015, **27**, 1316–1326.

52 Y. Wang, X. Liu, Y. Wang, H. Wang, H. Wang, S. L. Zhang, T. Zhao, M. Xu and Z. L. Wang, *ACS Nano*, 2021, **15**, 15700–15709.

53 W. Yuan, C. Zhang, B. Zhang, X. Wei, O. Yang, Y. Liu, L. He, S. Cui, J. Wang and Z. L. Wang, *Adv. Mater. Technol.*, 2021, **7**, 2101139.

54 H. Ouyang, Z. Liu, N. Li, B. Shi, Y. Zou, F. Xie, Y. Ma, Z. Li, H. Li, Q. Zheng, X. Qu, Y. Fan, Z. L. Wang, H. Zhang and Z. Li, *Nat. Commun.*, 2019, **10**, 1821.

55 N. Cui, L. Gu, Y. Lei, J. Liu, Y. Qin, X. Ma, Y. Hao and Z. L. Wang, *ACS Nano*, 2016, **10**, 6131–6138.

56 W. Seung, H. J. Yoon, T. Y. Kim, H. Ryu, J. Kim, J. H. Lee, J. H. Lee, S. Kim, Y. K. Park, Y. J. Park and S. W. Kim, *Adv. Energy Mater.*, 2016, **7**, 1600988.

57 Y. Zi, H. Guo, Z. Wen, M. H. Yeh, C. Hu and Z. L. Wang, *ACS Nano*, 2016, **10**, 4797–4805.

58 S. S. K. Mallineni, Y. Dong, H. Behlow, A. M. Rao and R. Podila, *Adv. Energy Mater.*, 2017, **8**, 1702736.

59 H. Kuang, S. Huang, C. Zhang, J. Chen, L. Shi, X. Zeng, Y. Li, Z. Yang, X. Wang, S. Dong, J. Yang, A. J. Flewitt and J. Luo, *ACS Appl. Mater. Interfaces*, 2022, **14**, 794–804.

60 L. Tang, X. Hui, J. Chen, H. Guo and F. Wu, *Nano Energy*, 2023, **118**, 109001.